



Subgrid-scale modelling of surface tension within interface tracking-based Large Eddy and Interface Simulation of 3D interfacial flows

Petar Liovic^{a,*}, Djamel Lakehal^b

^a Mathematics Informatics and Statistics Division, Commonwealth Scientific and Industrial Research Organization (CSIRO), Graham Road, Highett, VIC 3190, Australia

^b ASCOMP GmbH, Technoparkstrasse 1, Zürich, Switzerland

ARTICLE INFO

Article history:

Received 11 February 2011

Received in revised form 24 March 2012

Accepted 29 March 2012

Available online 20 April 2012

Keywords:

Surface tension

Volume-of-Fluid (VOF)

Large Eddy and Interface Simulation (LEIS)

ABSTRACT

This paper introduces a novel modelling procedure for unresolved surface tension in interface tracking-based Large Eddy and Interface Simulation (LEIS) of interfacial flows. The approach involves modelling of the subgrid-scale (SGS) surface tension appearing in the filtered momentum equation, and explicitly the dominant SGS curvature part of that term. The procedure for modelling the SGS curvature is based on the analysis of variations in curvature resulting from using different filter widths, as well from using alternative discretization-based and direct-filtering techniques for generating coarse-filter curvature estimates. Unresolved surface tension modelling can act to smooth spatial curvature variations and dampen parasitic modes, and can alternatively restore interface wrinkling when super-grid scale resolution underpredicts local curvature. The paper outlines the principles involved in identifying local regions of unresolved surface tension, and in constructing a model that is robust across the range of interface topologies. The current implementation is based on the height-function curvature discretization scheme in Volume-of-Fluid (VOF) interfacial flow simulations.

The procedure represents a SGS model in the true sense of the term – it is not a discretization scheme. The model should be used for Large Interface Simulation (LIS) of laminar interfacial flow modelling, too, complementing discretization schemes employed for resolved surface tension. Understandably the contribution of the model diminishes with mesh resolution as laminar flow does not continually introduce filter-scale interfacial deformations. The model may be more useful though for LEIS of turbulent interfacial flows, supporting discretization schemes for better capturing interface wrinkling, atomization and large bubble breakup.

© 2012 Elsevier Ltd. All rights reserved.

1. Introduction

The feasibility of small-scale interfacial flow modelling with finite-difference/volume (FD/FV) methods is highly dependent on the accuracy and stability of surface tension calculation. Documented methods for achieving surface tension modelling in Volume-of-Fluid (VOF) [16,28,29] and level set [34] flow simulations include the Continuum Surface Force (CSF) method [5], the Ghost Fluid Method (GFM) [11] and the Sharp Surface Force (SSF) method [12]) (among other approaches). For microfluidics and biomedical applications involving flows on the micron scale, parasitic modes resulting from errors in surface tension modelling can affect the results. In the case of Ultrasound Contrast Agent (UCA) microbubbles used clinically for imaging or therapeutic purposes [35], surface tension forces may be large relative to viscous stresses and inertia over much of their lifetime. Even under acoustic excitation, shape mode oscillations can result in multiple modes of devi-

ation from sphericity (“surface modes”), whether it be from the first-order oscillation [8] or from the longer-timescale second-order acoustic microstreaming [47]. Robustness of simulation and minimization of parasitic currents is served by using balanced-force multi-material flow solvers in conjunction with smooth curvature distributions [12,27]. Nevertheless, it is apparent that curvature smoothing may suppress full expression of shape mode oscillations in simulations of oscillating UCA microbubbles. The UCA microbubble example demonstrates that minimizing the loss of topological extrema as a result of curvature discretization is important. Such a priority in interfacial flow simulation, however, has typically been considered incompatible with curvature smoothing approaches for suppressing spurious extrema.

Beyond early curvature schemes involving direct differencing or convolution [5,46,39,55], the height function method [45] results in the most accurate estimates. Second- to fourth-order convergence could be obtained using height function-based curvature estimates [7,44]. In addition, increases in accuracy have been achieved using the smoothed partial derivatives in height function-based curvature estimation [31] and the orientation-independent height

* Corresponding author.

E-mail address: Petar.Liovic@csiro.au (P. Liovic).

function curvature scheme [27]. Unfortunately, higher-order accuracy in curvature discretization schemes only describes convergence approaching the continuum limit, and results in outcomes for absolute accuracy at lower mesh resolution ranging from minimal improvement to deterioration. In turbulent interfacial flow problems, high-order schemes and Adaptive Mesh Refinement (AMR) may be inadequate for preserving extrema in curvature distributions. In the LEIS of coastal wave breaking [26,30] and an air–water bubbling jet [25], surface wrinkling was found to be grid- and sub-grid scale because interface–turbulence interactions yield eddies cascading down from the bulk to individual wrinkles at the interface.

Smoothing out of local extrema in curvature distributions based on discretization is better appreciated by invoking the LEIS formalism [26,36,24]. More specifically, local errors in surface tension estimates may largely be due to inadequate interface resolution, introducing sub-grid scale contributions to curvature that cannot be captured by discretization on a mesh. When interface normals (thus curvature) are decomposed into super-grid and sub-grid scale components in LEIS, subsequent filtering of surface tension in the momentum equations yields a closure term for an “unresolved surface tension” [2,33,26,22,15]. In the present paper, we propose a model for SGS surface tension contributions. The proposed SGS curvature model is a “geometry-based” closure towards eliminating parasitic modes and capturing local curvature extrema, especially for significant spatial variations in surface topologies. For the class of interfacial flows dominated by surface or capillary forces, the way to eliminate parasitic modes and capture local curvature extrema is to invoke “physics-based” models (e.g. [18,19]) that introduce dissipative mechanisms via Kortoweg stresses. This is accomplished via the phase field theory or similarly using the double gradient hypothesis. The issue with these approaches is that they assume the flow to be driven by these Kortoweg stresses (capillary driven), and not by pressure, gravity or inertial forces as is generally the case in turbulent interfacial flows.

An SGS modelling route for representing surface tension in LEIS is introduced here as a more feasible means of promoting realistic and accurate capturing of interface deformation, fragmentation and coalescence than solely relying on finer mesh resolution. The model represents moving beyond establishing the need for explicit unresolved surface tension modelling, since filtering of the equations governing interfacial flow identifying additional terms beyond the SGS stress tensor for turbulence is now well established [26,49,30].

2. LEIS formalism

The equations governing multi-material flow are of course dependent on the number of material phases in the system. For illustrative purposes, it is more convenient to present the single-field formalism for multi-material flow based on the consideration of a system consisting of two fluids – liquid and gas. While much of the formalism presented here has been presented in previous works [23,25,26], it is useful to elucidate it here again, with an additional consideration of issues associated with flows featuring surface tension.

2.1. Continuum description

In the single-field formalism for Eulerian descriptions of gas–liquid flow, an indicator function is used to delineate points in space occupied by gas from points occupied by liquid. The simplest form of such a phase indicator function C is

$$C(\mathbf{x}, t) = \begin{cases} 1 & \text{if } \mathbf{x} \text{ occupied by phase } k = G, \\ 0 & \text{if } \mathbf{x} \text{ occupied by phase } k = L. \end{cases} \quad (1)$$

In the continuous limit, C is the Heaviside function. Fully-resolved solution to the gas–liquid flow involves time integration of the C distribution in a process known as *interface tracking*. Interface tracking involves solving the topology equation (in conservative form)

$$\frac{\partial C}{\partial t} + \nabla \cdot (C\mathbf{U}) = C\nabla \cdot \mathbf{U}. \quad (2)$$

In combination with definition of a C -weighted local density

$$\rho = C\rho_G + (1 - C)\rho_L, \quad (3)$$

Eq. (2) fulfills the governing equation describing species mass conservation in the gas–liquid flow

$$\frac{\partial \rho_S}{\partial t} + \nabla \cdot (\rho_S \mathbf{U}) = \rho_S \nabla \cdot \mathbf{U}, \quad (4)$$

where subscript S denotes fluid species. The aggregate result across the entire mixture of fluid species is total mass conservation:

$$\frac{\partial \rho}{\partial t} + \nabla \cdot (\rho \mathbf{U}) = \rho \nabla \cdot \mathbf{U}, \quad (5)$$

where all dependent variables are locally representative mixture-averaged quantities.

In incompressible flow, the equation of continuity

$$\nabla \cdot \mathbf{U} = 0 \quad (6)$$

reduces the RHS contributions of Eqs. (2), (4) and (5) to zero.

Again invoking locally representative mixture-averaged variables, the momentum equation for microscale description of the flow in the single-fluid formalism is

$$\frac{\partial \rho \mathbf{U}}{\partial t} + \nabla \cdot (\rho \mathbf{U} \mathbf{U}) = -\nabla P + \rho \mathbf{g} + \nabla \cdot \boldsymbol{\tau} + \gamma \kappa \hat{\mathbf{n}} \delta, \quad (7)$$

where P is the local pressure, \mathbf{g} is acceleration due to gravity, and $\boldsymbol{\tau}$ is the stress tensor.

The last term on the RHS is the surface tension force that is only non-zero at the interface (as determined by δ) and if the surface tension γ is non-zero. The surface tension force is dependent on interface orientation $\hat{\mathbf{n}}$ and interface curvature κ . The former is a first-derivative of interface location

$$\hat{\mathbf{n}} = \frac{\nabla C}{|\nabla C|}, \quad (8)$$

while the latter requires second-derivatives of interface location

$$\kappa = \nabla \cdot \hat{\mathbf{n}} = \nabla \cdot \frac{\nabla C}{|\nabla C|}. \quad (9)$$

2.2. LEIS and filtered single-field formalism

Incompressible single or multi-phase flow features a spectrum of length scales that depends on the Reynolds number, Re . For very high Re flows, the mesh is in practice insufficient to resolve the smallest length scales. If the smallest length scales cannot be systematically resolved by the grid, their coupling with the super-grid or resolved-scale solution needs to be modelled. Consistent with the LES concept for single-phase turbulent flow, the filtering of the equations governing two-fluid flow is only done spatially (and not spatially-and-temporally).

More precisely, all dependent flow variables are decomposed into resolved- and subgrid-scale (SGS) components. Filtering of the color function C using

$$\bar{C}(\mathbf{x}, t) \equiv G \otimes C = \int_D G(\mathbf{x} - \mathbf{x}') C(\mathbf{x}', t) d\mathbf{x}', \quad (10)$$

transforms the Heaviside-step indicator function into a resolved phase volume fraction. In the Eulerian description, the interface is

embedded at any instant in time within the spatial distribution $\bar{C}(x, y, z)$ as regions of $0 < C < 1$. Of the many filters that are used in LES (refer to e.g. [40]), the tophat filter within the finite volume context is commonly used. Filtering Eq. (2) and enforcing incompressibility yields

$$\frac{\partial \bar{C}}{\partial t} + \nabla \cdot (\bar{C} \mathbf{U}) = 0, \quad (11)$$

which is directly discretized by volume fluxes when VOF interface tracking is used. Appendix A discusses in more detail the consequences of this filtering outcome for interface tracking in multi-fluid flow simulation using LEIS.

As well as coupling into the momentum equation through C-weighted bulk property distributions, the solution to the interface location should also impact on the flow field solution by enforcing continuity of momentum through fulfillment of the jump conditions

$$[\tau_N] = [P] + \sigma \kappa, \quad (12)$$

$$[\tau_S] = 0, \quad (13)$$

where Eqs. (12) and (13) are the normal and tangential stress balances, respectively.

With filtering applied on a term-by-term basis, care should be taken to ensure that the filtering preserves the fundamental properties of conservation, linearity and commutation with derivation [40], even in the interface regions. The most obvious means for LEIS to best fulfill these properties is through the use of the density-based Component-Weighted Volume Averaging (CWVA) to complete the coupling [23]:

$$\tilde{f} = \frac{\bar{\rho} \tilde{f}}{\bar{\rho}}, \quad (14)$$

which is analogous to Favre averaging for variable-density flow. (Favre averaging has historically been applied to compressible flows, and is readily extensible once the assumption of incompressibility is relaxed.) Applying CWVA to Eq. (7) yields the filtered momentum equations [25,26]

$$\frac{\partial \bar{\rho} \tilde{\mathbf{U}}}{\partial t} + \nabla \cdot (\bar{\rho} \tilde{\mathbf{U}} \tilde{\mathbf{U}}) = -\nabla \cdot (\bar{\Pi} - \tau^{SGS}) + \gamma \bar{\kappa} \tilde{\mathbf{n}} \delta + \bar{\rho} \mathbf{g} + \epsilon_c + \epsilon_d + \epsilon_\gamma, \quad (15)$$

where ϵ_k are the additional filtering-induced terms. Of particular note is the fourth closure term

$$\epsilon_\gamma = \gamma \bar{\kappa} \tilde{\mathbf{n}} \delta - \gamma \bar{\kappa} \tilde{\mathbf{n}} \delta, \quad (16)$$

denoting the unresolved surface tension. This term is non-negligible in a range of multiphase flows. A *priori* analysis by Liovic and Lakehal [26] showed the closure term for unresolved surface tension to be important relative to the SGS stress term primarily in regions of the flow featuring interfaces that are poorly resolved. The more familiar turbulence SGS stress term reads

$$\tau^{SGS} = \rho(\tilde{\mathbf{U}} \tilde{\mathbf{U}} - \tilde{\mathbf{U}} \tilde{\mathbf{U}}). \quad (17)$$

[The addition of “interface” into the label LEIS refers to the fact that the “Direct Numerical Simulation (DNS) of multi-fluid flow” is not achieved if terms such as those in Eqs. (17) and (16) are not negligible, especially if the observed convergence of a flow solver does not match that prescribed by its formal order of accuracy. Understandably, if the flow is laminar from a turbulence viewpoint there is no SGS motion, meaning that $\tau^{SGS} = 0$. Such a situation, however, does not automatically mean that ϵ_γ is also zero. In such cases, the flow simulation is no longer LEIS, but rather degenerates to Large Interface Simulation (LIS).]

3. Surface tension modelling in LEIS

Numerical discretization for LEIS involves consideration of Eqs. (11) and (15). The filtering outcome in Eq. (11) – specifically the fact that upon filtering the phase indicator takes the form of a volume fraction indicator function – established Volume of Fluid (VOF) as the interface tracking method of choice for LEIS in the current work. The current study uses the MFVOF-3D software [25,26,30] for LEIS of 3D interfacial flows. MFVOF-3D features a combination of conservative finite-difference and finite-volume schemes for multi-material flow simulation. Interface tracking is achieved by using geometric VOF methods [28,29] that are resolved on a twice-as-fine sub-mesh nested within the underlying flow solver mesh. The use of a twice-as-fine mesh for VOF computations in the MFVOF-3D LEIS code enables interfacial volume flux reconstructions generated by the VOF interface tracking module to be used for computing momentum fluxes and bulk property distributions, and to an extent counters the interface-smearing action of filtering (e.g. CWVA). The geometry-based computation of fluxes and local density estimates (described in more detail in [26]) is particularly important to the LEIS flow solver. The control of mass-residual errors in a LEIS flow solver based on the filtered multi-material flow equations is promoted by fluid densities remaining as constant as possible over particle trajectories. Of the interface tracking methods, it is indeed VOF that explicitly computes fluxes as geometrically reconstructed fluid parcels, which means that fluid particles do not cross the interface but rather cause the interface to advect. The MFVOF-3D code is also well suited to performing LEIS, because of its interface-cognizant SGS stress tensor modelling [26,30], its advanced algorithms for solving elliptic linear problems in flow solution algorithms [27], and because of its subdomain-based parallelization and ability to run on parallel supercomputers.

3.1. Surface tension force discretization

Coincidentally, VOF-based descriptions of the interface form the basis of the original Continuum Surface Force (CSF) method [5] used for incorporating surface tension effects into mesh-based multi-material flow simulation. The CSF method introduced a kernel width for mimicking the effect of the delta function in the surface tension term $\gamma \kappa \mathbf{n} \delta$. Given a VOF C-based representation of the interface, Brackbill *et al.* [5] derived the surface tension force to be

$$\lim_{\Delta \rightarrow 0} \gamma \kappa \mathbf{n} \delta = \gamma \kappa \nabla C, \quad (18)$$

which is discretized (for the example of the $(i + 1/2, j, k)$ point) as

$$\mathbf{F}_{STENSIONx}|_{i+1/2,j,k} = \gamma \kappa_{i+1/2,j,k} \frac{\partial C}{\partial x} \Big|_{i+1/2,j,k}. \quad (19)$$

More recently, Francois *et al.* [12] have introduced the Sharp Surface Force (SSF) method – a Ghost Fluid-inspired approach in which the force is computed only at velocity locations on the staggered meshes at both sides of the interface. For the same $(i + 1/2, j, k)$ point,

$$\mathbf{F}_{STENSIONx}|_{i+1/2,j,k} = \pm \frac{\gamma \kappa_l}{\delta x_{i+1/2}}, \quad (20)$$

with the sign depending in which side of the interface the mesh point lay. With the use of VOF interface reconstructions for the reconstruction of sharp momentum fluxes using VOF-augmented momentum advection [26], the SSF method results in sharper reproduction of the pressure jump at the interfaces of bubbles/drops in static equilibrium. As such, the SSF method is preferred

for use in multi-material simulation of interfacial flows, and is used in the current work.

3.2. Curvature computation

Curvature estimation has long been the main shortcoming in surface tension modelling in interface-tracking-based flow simulations. Many works have shown the superiority of curvature estimation using a “height function” approach, with height functions generated either from VOF data [45,7,12,27,31], or Level-Set data [44,43,27]. The height function approach effectively parameterizes the interface: for example, given the height function definition in the x -direction, the subsequent formula for curvature in 3D Cartesian space

$$\kappa = -\frac{h_{yy} + h_{zz} + h_{yy} + h_{yy}h_z^2 + h_{zz}h_y^2 - 2h_{yz}h_yh_z}{(1 + h_y^2 + h_z^2)^{3/2}}, \quad (21)$$

does not feature derivatives in the x -direction. In that case, as long as the mean interface normal is essentially perpendicular to the yz -plane, transverse variations in h in the curvature stencil remain small and well approximated by discrete gradient operators. The height function is a significant improvement on past finite-differencing or convolution-based curvature schemes that involved computing of derivatives based on discrete operators applied across the contact discontinuity that the steep-to-sharp variation in C is supposed to represent.

3.3. SGS modelling of unresolved surface tension

A priori analysis of LEIS simulation flow field outputs for turbulent flow around a gas bubble rising in a quiescent liquid [26] showed the magnitude of the unresolved surface tension to often be unimportant relative to the turbulence counterpart (SGS stresses) in various regions of the flow. Cases of relatively poor interface resolution increase the magnitude of unresolved curvature contributions, while flow relaminarization reduces the magnitude of the SGS stresses; both act to increase the relative importance of unresolved surface tension.

Even though the unresolved surface tension term (Eq. (16)) was identified through filtering only in the last decade, it is surprising that so little progress has been made to date in obtaining a verified, practical closure for it. Along with filtering the single-field representation of multi-material flow to identify the unresolved surface tension term for closure, Alajbegovic [2] also proposed a general form of an SGS model of unresolved surface tension that was linked to the SGS turbulence scales. The proposed modelling framework was never documented as being further developed or tested as a specific SGS model. The justification in [2] for the linkage of SGS surface tension and stresses is also not obvious, given that the curvature (resolved or SGS) is specifically a property of interface topology. This is because unresolved surface tension can also manifest itself in laminar interfacial flows, and hence should not be linked to nonexistent turbulence characteristics. Herrmann and Gorokhovski [15] proposed explicit filtering based on knowledge of “exact” curvatures and normals, with the approach relying on a refined Level-Set method to represent the exact interface. While potentially useful for some subsets of multi-material flow scenarios, the use of refinement-based techniques limits its widespread applicability. The general assumption of smooth level sets for surface tension modelling in flow computations using Level-Set interface tracking has also been shown to be presumptuous and often incorrect [32]. These factors suggest that a substantial validation and optimization effort is required before the refined Level-Set Exact-Curvature approach can be considered feasible for practical computations.

In this work, we propose an alternative approach to modelling unresolved surface tension based on surface topology representation on an additional coarse-grid. In this way the approach becomes a true SGS modelling strategy, in contrast to the use of interface representations on a (significantly) finer-grid (such as the concept described in [15]) that would be better described as simulation-based SGS reconstruction. In LEIS, dependent variables are implicitly filtered by the process of spatial discretization, which is equivalent to using a top-hat filter with a mesh-dependent width. In the CSF formulation, the surface tension force consists of two variables – κ and \hat{n} – that are derived from the interface representation; these derived variables consist of resolved-scale (“supergrid”) and subgrid contributions, i.e.

$$\kappa = \bar{\kappa} + \kappa^{SGS}, \quad (22)$$

$$\hat{n}_i = \bar{\hat{n}}_i + \hat{n}_i^{SGS}. \quad (23)$$

The filtered surface tension force can be derived using these decompositions:

$$\gamma \bar{\kappa} \bar{\hat{n}}_i \delta = \gamma (\bar{\kappa} + \kappa^{SGS}) (\bar{\hat{n}}_i + \hat{n}_i^{SGS}) \delta. \quad (24)$$

By analogy with conventional LES methodology, one possible LEIS approach to SGS modelling is to use the supergrid distributions to compute the resolved surface force $\gamma \bar{\kappa} \bar{\hat{n}}_i \delta$, and then model the unresolved surface force term (Eq. (16)). Alternatively, the current work presents a procedure for interrogating interface geometry that enables κ^{SGS} and \hat{n}^{SGS} to be modelled separately and inserted directly into Eq. (24). For a multi-material flow solver featuring a SSF/GFM treatment of surface tension within a balanced-force multi-material flow solver, the interface normal does not appear in Eq. (20) and so is not used. In that case Eq. (23) is ignored, and the entire effort of SGS modelling of surface tension is focused on modelling the SGS curvature. Equating of SGS surface tension modelling with SGS curvature modelling is also sensible because (unlike the interface normal) curvature is the second-derivative of interface location and hence prone to aliasing error [7].

3.4. Discretization versus explicit filtering

A starting point for modelling SGS curvatures and interface normals is to recognize that there are two alternative routes towards a coarse-filtered curvature estimate from an interface representation on a regular mesh: (i) compute the curvature from discretization on the regular mesh, then explicitly apply a coarse filter to the curvature distribution; (ii) explicitly apply a coarse filter to the interface representation, then input the coarse-filtered interface representation into a curvature discretization scheme. We denote a 2Δ -filtered curvature based on direct filtering of the super-grid curvature as $\bar{\kappa}^{2\Delta}$, and a 2Δ -filtered curvature based on discretization using a 2Δ -filtered interface representation as $\kappa^{\bar{C}(2\Delta)}$ (and similar for filter width 3Δ). The computation of each expression is done as follows.

3.4.1. Discretization-based curvature: $\kappa^{\bar{C}(n\Delta)}$

The use of C in the superscript denotes interface representation, but should not be further interpreted as implying that the discretization-based curvature is based on direct finite-differencing of the color function C . In the current work, the underlying interface representation using C is locally parameterized by introducing the height function. For clarity of explanation, the case of an interface with a dominant n_x interface normal component is considered here. From C on the regular mesh, the height function is computed at an interface segment featuring dominance of interface normal component n_x as

$$h_{j,k} = \sum_{ii=-i_{radius}}^{i_{radius}} C_{i+ii,j,k} \delta x_{i+ii}. \quad (25)$$

The height function for surface tension curvature schemes is usually documented (e.g. in [12]) to involve use of a $7 \times 3 \times 3$ stencil, which is equivalent to the bounds $-3 \geq ii \geq 3$ in Eq. (25). These bounds need not be rigidly set: in reality, the i -extent of the stencil should be small enough to ensure that the interface does not cross (j,k) -row borders more than once (avoid the interface folding back on itself), and large enough for all (j,k) -row borders to be crossed at least once (full capturing of interface within the local stencil). Given the local height function, the curvature is computed by discretizing Eq. (21). Second-order centered differences applied to Eq. (21) yield the discretization formula for curvature as

$$\kappa_{i,j,k}^{(n\Delta)} = \frac{h_{yy}|_{n\Delta} + h_{zz}|_{n\Delta} + h_{yy}|_{n\Delta}(h_z|_{n\Delta})^2 + h_{zz}|_{n\Delta}(h_y|_{n\Delta})^2 + 2h_{yz}|_{n\Delta}h_y|_{n\Delta}h_z|_{n\Delta}}{(1 + (h_y|_{n\Delta})^2 + (h_z|_{n\Delta})^2)^{3/2}}, \quad (26)$$

where

$$h_y|_{n\Delta} = \frac{h_{n,0} - h_{-n,0}}{2n\delta y}, \quad (27)$$

$$h_z|_{n\Delta} = \frac{h_{0,n} - h_{0,-n}}{2n\delta z}, \quad (28)$$

$$h_{yy}|_{n\Delta} = \frac{h_{n,0} - 2h_{0,0} + h_{-n,0}}{(n\delta y)^2}, \quad (29)$$

$$h_{zz}|_{n\Delta} = \frac{h_{0,n} - 2h_{0,0} + h_{0,-n}}{(n\delta z)^2}, \quad (30)$$

$$h_{yz}|_{n\Delta} = \frac{h_{n,n} - h_{n,-n} - h_{-n,n} + h_{-n,-n}}{(2n\delta y)(2n\delta z)}. \quad (31)$$

For the discretization-based curvatures, a $(2n+1) \times (2n+1) \times (2k_{radius}+1)$ stencil of regular-mesh C data about cell (i, j, k) is input into the curvature discretization scheme, and the scheme generates $h_{j,k}$ over a $(2n+1) \times (2n+1)$ regular 2D mesh in the local yz -plane. In the current work, $k_{radius} = 5$ at the widest filter width 3Δ to yield a $7 \times 7 \times 11$ stencil; stencil length k_{radius} is made sufficient for increased accuracy of height function estimates in the “near-45°” interface orientation scenario [31] and given the wider height function target stencil can yield greater change in height over the width of the C input stencil. To compute $\kappa_{i,j,k}^{(n\Delta)}$, $\kappa_{i,j,k}^{(3\Delta)}$ and $\kappa_{i,j,k}^{(2\Delta)}$, the discretization spacing is made consecutively bigger using the factor n . The “coarse-filtering of the interface representation” refers only to the curvature discretization formulae (Eqs. (26)–(31)) ignoring variations in height function between the points in the height function stencil used in the formulae; no explicit filtering of the height function or the precursor C distribution is performed. Fig. 1a shows an illustrative example of the implicit filtering achieved by discretization when successively coarser discretization spacings are used in the height function-based curvature computation. In particular, the figure shows the potential for mesh-scale curvature contributions within the stencil to be bypassed by Eqs. (26)–(31) due to the use of coarser discretization.

3.4.2. “Direct-filtering” curvature: $\bar{\kappa}^{n\Delta}$

Having generated the curvature estimate based on the regular-mesh discretization $\kappa(\equiv \kappa^{(n\Delta)})$, explicitly coarse-filtered curvature estimates can subsequently be generated by convolution with a conventional spatial filter. In implementation, the direct-filtering curvature estimate takes the form

$$\bar{\kappa}_{i,j,k}^{n\Delta} = \sum_{kk=-k_{radius}}^{k_{radius}} \sum_{jj=-j_{radius}}^{j_{radius}} \sum_{ii=-i_{radius}}^{i_{radius}} \omega_{ii,jj,kk} \kappa_{i+ii,j+jj,k+kk}, \quad (32)$$

where the $2i_{radius}+1 \times 2j_{radius}+1 \times 2k_{radius}+1$ stencil of regular-mesh curvature values is large enough to accommodate all significant non-zero weights ω generated by using a filter wider than the mesh

spacing. Fig. 1b shows the support for explicit filtering of the local regular-mesh curvature distribution if a top-hat filter is applied. In the current work, the Gaussian filter [40]

$$G(\mathbf{x} - \mathbf{x}') = \sqrt{\frac{6}{\pi\Delta^2}} \exp\left(-\frac{6|\mathbf{x} - \mathbf{x}'|^2}{\Delta^2}\right) \quad (33)$$

is used to illustrate generality with regard to filter choice; other filters can also be used. For coarse-filtered curvature estimates, consecutively wider filter widths 2Δ and 3Δ replace Δ in Eq. (33). In contrast to the example in Fig. 1a, the filtering operations over the stencils in Fig. 1b can ensure that mesh-scale interface curvatures within the support are not bypassed and actually make non-negligible contributions to smoothed curvature outputs. On the other hand, locally smooth curvature variations that should be captured in curvature estimates may be polluted in the direct-filtering case by off-centre contributions from within wider filtering supports.

3.5. A procedure for SGS surface tension modelling

In principle, separate models are required for the SGS curvature and for the SGS interface normal components. Presentation and discussion of the new SGS model is initially done here for the more important SGS curvature, with assurance that the modelling principles are extensible to the SGS interface normal case as well. The new SGS curvature model is better described as a procedure, since model outputs are based on local field analysis and heuristic delineation of case-based scenarios. In essence, the SGS curvature procedure involves the continuation of trends in curvature variation that are consistent over successive filter widths, and the imposition of “most sensible” curvatures if inconsistency in variation is seen over the successive filter widths.

3.5.1. Geometric visualization of SGS curvature

A starting point for a solely topology-based SGS curvature model is the analysis of variations in discretization-based curvature estimates by progressively narrowing the filter width. The output of Eq. (26) tending towards saturation with reduction in stencil width n is strong evidence of the presence of SGS curvature, separate from any other sources of curvature discretization error. When saturation is made evident using implicit filters wider than the mesh scale (discretizations using $n > 1$),

$$\left| \kappa_{i,j,k}^{((n+2)\Delta)} - \kappa_{i,j,k}^{exact} \right| > \left| \kappa_{i,j,k}^{((n+1)\Delta)} - \kappa_{i,j,k}^{exact} \right| > \left| \kappa_{i,j,k}^{(n\Delta)} - \kappa_{i,j,k}^{exact} \right| \approx \left| \kappa_{i,j,k}^{(n\Delta)} - \kappa_{i,j,k}^{exact} \right| \approx 0 \quad (34)$$

holds. When saturation is not approached by using successively finer filters down to a filter width corresponding to the mesh scale, i.e.

$$\left| \kappa_{i,j,k}^{(4\Delta)} - \kappa_{i,j,k}^{exact} \right| > \left| \kappa_{i,j,k}^{(3\Delta)} - \kappa_{i,j,k}^{exact} \right| > \left| \kappa_{i,j,k}^{(2\Delta)} - \kappa_{i,j,k}^{exact} \right| > \left| \kappa_{i,j,k}^{(\Delta)} - \kappa_{i,j,k}^{exact} \right| \gg 0 \quad (35)$$

modelling of the saturation of the curvature is required to obtain κ^{SGS} . Explicitly identifying trends such as Eq. (35) is a key part of the SGS curvature procedure. The geometric visualization of the trends of Eqs. (34) and (35) is given in Fig. 2. In the example of Fig. 2a, the regular-mesh curvature estimate $\kappa^{(n\Delta)}$ is smaller than the coarse-filtered discretized curvature $\kappa^{(2\Delta)}$. In the absence of undetected inflections in curvature along the interface segment, the bulk of the contribution to the magnitude $\kappa^{(2\Delta)}$ appears from the parts of the wider stencil not overlapped by the regular stencil, and the centre of the stencil is a relatively low-curvature zone:

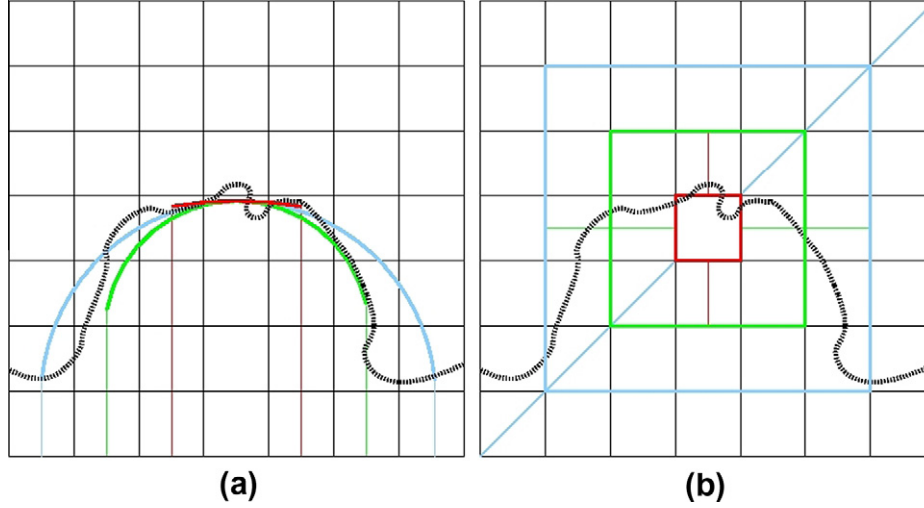


Fig. 1. Stencils for coarse-filtered curvature estimates. “Discretization-based” filtering of the interface representation takes the form of coarsening the discretization spacing in the second-order accurate height function-based finite-difference formula, as shown in panel (a). “Direct filtering”, on the other hand, involves using height function-based regular-mesh curvature estimate distributions, and subsequently applying filters wider than the mesh spacing (shown in panel (b)). Lines of different shading highlight the use of the different filter widths (1Δ , 2Δ and 3Δ).

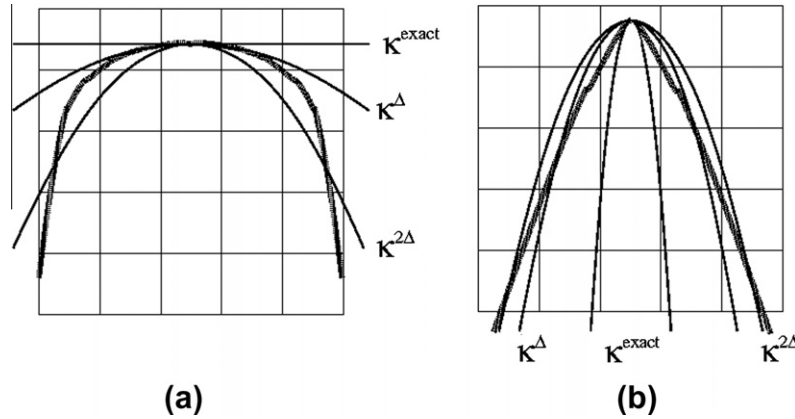


Fig. 2. Geometric visualization of consistent trends in curvature estimates: (a) exact curvature flatter than discretization-based curvatures computed using Δ and 2Δ mesh spacings in Eq. (26); (b) exact curvature steeper. (Labels are located next to their corresponding lines.)

$$\lim_{n \rightarrow 0} \bar{\kappa}_{ij,k}^{(n\Delta)} < \bar{\kappa}_{ij,k}^{(\Delta)}, \quad (36)$$

such that $\kappa^{SGS} < 0$. Similarly, Fig. 2b for a protruding finger shows $\bar{\kappa}_{ij,k}^{(\Delta)} > \bar{\kappa}_{ij,k}^{(2\Delta)}$, such that

$$\lim_{n \rightarrow 0} \bar{\kappa}_{ij,k}^{(n\Delta)} > \bar{\kappa}_{ij,k}^{(\Delta)}. \quad (37)$$

In this case $\kappa^{SGS} > 0$, inviting modelling to add subgrid-scale interface wrinkling to compensate for small interfacial length-scale detail that discretization cannot capture.

With enough successive filter widths, reliably convergent curvature discretization schemes and moderate refinement, modelling saturation to the exact curvature can be viewed as an extrapolation process and can utilize a range of off-the-shelf extrapolation techniques. In reality, algorithmic robustness requirements impose practical upper limits on stencil size (e.g. columns for defining height functions not featuring multiple interface segments). We consider $1 \geq n \geq 3$ to flag the range of data available for identifying trends that fulfill Eq. (35). For $n_{max} = 3$, modelling of the saturation is necessarily more heuristics-based and conservative in its effect on the predicted κ^{SGS} .

3.5.2. SGS curvature versus general discretization error: consistency of curvature variation

Variations in discretization-based curvature estimates with consistently varying filter width such as those described by Eq. (35) make up some subset of all variations for all mixed cells ($0 < C < 1$). In other cases, the variations are nowhere near as systematic, so that trends towards saturation of the curvature estimate with reducing filter width cannot be identified. Convergence of any data with increasing mesh refinement may be oscillatory rather than monotonic, in which case estimates from only three consecutive mesh spacings are totally inadequate for modelling saturation. A scenario more unique to interfacial flow simulation is that curvature estimates from three consecutively finer mesh spacings may diverge, due to new interfacial length scales appearing at finer mesh spacings, or instances of poor behaviour by curvature discretization schemes. The net error in discretization-based curvature can consist of a height function discretization error (from Eq. (25)) and an error associated with the curvature discretization formula (Eqs. (26)–(31)). Non-systematic variations in the discretization-based curvature estimates due to such factors complicate efforts to correctly attribute as much of

the discretization error as possible to SGS curvature contributions.

Variations in discretization-based curvature estimates often do not exhibit a tendency towards saturation, so that curvature variation with filter width from the geometric perspective is not easily extrapolated to the infinitesimal filter length limit. For that reason, it is useful to additionally consider curvature estimates from sources other than discretization. As an alternative approach to analyzing variations in discretization-based curvature estimates, we propose to compare them with equivalent estimates from curvatures obtained by direct filtering. Curvature estimates obtained by direct filtering using coarser filters are used to prove consistency of variation in discretization-based curvature estimates. Moreover, if consistency of discretization-based curvature estimate variation cannot be proven, the direct-filtering curvature estimates increases the pool of estimates from which to model the exact curvature. In such cases, the regular-mesh estimate may be overridden by the new estimate, thereby making κ^{SGS} locally more substantial. The potential of such an approach for detecting and eliminating parasitic modes in local curvature distributions on surfaces is obvious.

3.5.3. Model heuristics and parameters

The heuristics prescribed here are based on testing experience in the analysis of variations in discretization-based and direct-filtering curvature estimates within compact stencils. The model parameters used in the heuristics have been chosen based on accuracy gains achieved in testing across a range of mesh resolutions. In the current study, two different model procedures are presented, using different detection criteria and formulae for SGS curvature computation. The two different models differ in peak performance at any resolution, and in averaged performance over an adequately large resolution range. In presenting two different SGS curvature models, it should be clear to the reader that the potential for larger gains is significant. This is aided by the ease with which model settings can be changed once the correct infrastructure for computing discretization-based curvatures from height functions and direct-filtering curvature estimates is in place.

3.5.3.1. SGS curvature Model 1: conservative wrinkling. In the first SGS curvature model procedure, there are only five different cases of curvature variation across filter scales to consider, of which only one case results in increased wrinkling.

Case 1: Constant curvature.

Constant curvature is indicative of equilibrium interface configurations. Given good interface resolution by the local mesh and using convergent discretization numerics, a narrow band on both discretization-based and direct-filtering curvature estimates verifies locally constant curvature. Once the narrow band has been verified, using $\bar{\kappa}_{ij,k}^{3\Delta}$ results in local smoothing of parasitic modes. The criterion

$$\max \left(\begin{array}{l} \left| \kappa_{ij,k}^{\bar{C}(2\Delta)} - \kappa_{ij,k}^{\bar{C}(3\Delta)} \right|, \left| \kappa_{ij,k}^{\bar{C}(2\Delta)} - \bar{\kappa}_{ij,k}^{2\Delta} \right|, \left| \kappa_{ij,k}^{\bar{C}(2\Delta)} - \bar{\kappa}_{ij,k}^{3\Delta} \right|, \\ \left| \kappa_{ij,k}^{\bar{C}(3\Delta)} - \bar{\kappa}_{ij,k}^{2\Delta} \right|, \left| \kappa_{ij,k}^{\bar{C}(3\Delta)} - \bar{\kappa}_{ij,k}^{3\Delta} \right|, \left| \bar{\kappa}_{ij,k}^{2\Delta} - \bar{\kappa}_{ij,k}^{3\Delta} \right| \end{array} \right) < a \left| \kappa_{ij,k}^{\bar{C}(\Delta)} \right| \quad (38)$$

is used to identify cases of constant curvature.

Case 2: Consistent variation.

One means of verifying truly consistent curvature variation with decreasing filter width is based on the trend in the discretization-based curvature estimates described by Eq. (35) being matched by the same trend in the direct-filtering estimates. Provided other cases associated with “non-consistent” discretization-based curvature variation are not fulfilled beforehand, fulfillment of

$$\left| \kappa_{ij,k}^{\bar{C}(\Delta)} \right| > \left| \kappa_{ij,k}^{\bar{C}(2\Delta)} \right| \quad (39)$$

and

$$\left| \kappa_{ij,k}^{\bar{C}(\Delta)} \right| > \left| \bar{\kappa}_{ij,k}^{2\Delta} \right| \quad (40)$$

is used in the procedure to indicate that $\kappa_{ij,k}^{\bar{C}(\Delta)}$ underpredicts the exact curvature, and $\left| \kappa_{ij,k}^{SGS} \right|$ should act to add wrinkling to the local curvature estimate. Similarly, fulfillment of

$$\left| \kappa_{ij,k}^{\bar{C}(\Delta)} \right| < \left| \bar{\kappa}_{ij,k}^{2\Delta} \right| \quad (41)$$

and

$$\left| \kappa_{ij,k}^{\bar{C}(\Delta)} \right| < \left| \bar{\kappa}_{ij,k}^{2\Delta} \right| \quad (42)$$

can be used in the procedure to indicate that $\kappa_{ij,k}^{\bar{C}(\Delta)}$ overstates the magnitude of the curvature, and $\left| \kappa_{ij,k}^{SGS} \right|$ should act to reduce the net (unfiltered) curvature estimate. In the current work, this second effect for prescribing a reduction in net curvature is neglected, since these contributions are smaller and are bound in the methodology by $\kappa = 0$.

In this consistent variation case, variations in discretization-based curvature are assumed to be geometrically sensible, and $\kappa_{ij,k}^{SGS}$ is constructed based on magnitudes of deviations from the regular curvature estimate $\kappa_{ij,k}^{\bar{C}(\Delta)}$ (rather than an override of the regular-mesh discretization-based estimate).

Case 3: Inconsistency in variations between different curvature estimates.

Three successive filter widths matching the trend in Eq. (35) with a similar trend in the direct filtering-based curvatures is a useful indicator of consistent variation in curvature with decreasing filter width. One indicator of inconsistency is given by identifying a change in the type of curvature estimate (discretization or direct filtering) that is bigger at a particular coarser filter width. If

$$\left| \kappa_{ij,k}^{\bar{C}(3\Delta)} \right| > \left| \bar{\kappa}_{ij,k}^{3\Delta} \right|, \quad (43)$$

$$\left| \kappa_{ij,k}^{\bar{C}(2\Delta)} \right| < \left| \bar{\kappa}_{ij,k}^{2\Delta} \right|, \quad (44)$$

or

$$\left| \kappa_{ij,k}^{\bar{C}(3\Delta)} \right| < \left| \bar{\kappa}_{ij,k}^{3\Delta} \right|, \quad (45)$$

$$\left| \kappa_{ij,k}^{\bar{C}(2\Delta)} \right| > \left| \bar{\kappa}_{ij,k}^{2\Delta} \right|, \quad (46)$$

then the variations in curvature are considered to be inconsistent. In addition, inconsistency may be indicated by a substantial mismatch in the curvature estimates between different filter widths. The ratio of coarse-filtered discretization-based curvature estimates are related as

$$\left| \kappa_{ij,k}^{\bar{C}(3\Delta)} \right| = \left| b_1 \kappa_{ij,k}^{\bar{C}(2\Delta)} \right|, \quad (47)$$

and similarly the direct-filtering curvature estimates are related as

$$\left| \bar{\kappa}_{ij,k}^{3\Delta} \right| = \left| b_2 \bar{\kappa}_{ij,k}^{2\Delta} \right|. \quad (48)$$

In the case of geometrically consistent variations in curvature, ratios b_1 and b_2 will be similar. A large difference between b_1 and b_2 has been found to be a good indicator of inconsistency in curvature variation in the geometric sense. This points to the presence of substantial non-zero SGS curvature somewhere in the dense stencil of direct filtering (not necessarily at point (i, j, k)) that is noticed by the direct filtering but bypassed by the discretization-based approach to curvature estimation. If any of these Case 3 indicators of inconsistency are fulfilled, then an override of the regular-mesh discretization-based estimate may be prescribed. The choice of

candidate from a subset of the total pool of candidates is heuristic, and in the current work is chosen from the pool to minimize the magnitude of the curvature estimate.

Case 4: Pinch at intermediate filter width.

Case 3 in itself broadly encompasses much of the perceived inconsistency, yet only prescribes one treatment. It is desirable for us to be able to identify additional cases that include subsets of Case 3, for which heuristics based on more realistic overrides of $\kappa_{ij,k}^{(\Delta)}$ can be prescribed. One such case can be identified based on near-equality between discretization-based and direct filtering-based curvatures using the 2Δ filter width, but substantial difference between the different estimates at the 3Δ filter width, i.e. identifying a pinch at 2Δ :

$$\left| \kappa_{ij,k}^{(\bar{C}(3\Delta))} - \bar{\kappa}_{ij,k}^{3\Delta} \right| > c_1 \kappa_{ij,k}^{(\bar{C}(3\Delta))}, \quad (49)$$

$$\left| \kappa_{ij,k}^{(\bar{C}(2\Delta))} - \bar{\kappa}_{ij,k}^{2\Delta} \right| < c_2 \kappa_{ij,k}^{(\bar{C}(2\Delta))}, \quad (50)$$

where $c_1 \gg c_2$. In this case, it is sensible to assume that the bulk of the difference between $\kappa_{ij,k}^{(\bar{C}(3\Delta))}$ and $\bar{\kappa}_{ij,k}^{3\Delta}$ is due to curvature contributions within the 3Δ support not overlapped by the 2Δ support. **Condition 49** precludes the invocation of Case 1, on the basis that discretization-based and direct-filtering estimates diverging with decreasing filter width suggest the regular-mesh $\kappa_{ij,k}^{(\Delta)}$ to be unreliable. An average of the direct-filtered and discretization-based values at the 3Δ filter width has been seen to result in better outcomes than the draconian prescription of Case 3. In effect, the contributions at the center of the filter are least trusted, and hence best diluted in this case across as coarse a filter width as practicable.

Case 5: Pinch across both coarser filters.

Another useful case worth identifying is that of near-equality between discretization-based and direct filtering-based curvatures using the 2Δ and 3Δ filter widths, but both of them different to the estimate at the Δ filter width, i.e. identifying a broad pinch across all coarser filters:

$$\left| \kappa_{ij,k}^{(\bar{C}(3\Delta))} - \bar{\kappa}_{ij,k}^{2\Delta} \right| < \left| d_1 \left(\kappa_{ij,k}^{(\bar{C}(3\Delta))} + \kappa_{ij,k}^{(\bar{C}(2\Delta))} \right) / 2 \right|, \quad (51)$$

$$\left| \bar{\kappa}_{ij,k}^{3\Delta} - \bar{\kappa}_{ij,k}^{2\Delta} \right| < \left| d_2 \left(\bar{\kappa}_{ij,k}^{3\Delta} + \bar{\kappa}_{ij,k}^{2\Delta} \right) / 2 \right|, \quad (52)$$

$$\left| \kappa_{ij,k}^{(\bar{C}(2\Delta))} - \bar{\kappa}_{ij,k}^{\Delta} \right| > \left| d_3 \left(\kappa_{ij,k}^{(\bar{C}(2\Delta))} + \kappa_{ij,k}^{(\bar{C}(\Delta))} \right) / 2 \right|, \quad (53)$$

where $d_3 \gg d_1, d_2$. In this case, the pinch and the contributions from nearer to the center of the filter support are considered to be more reliable than in Case 4, hence motivating an override based on the direct-filtering estimates using the Δ and 2Δ filter widths.

Summary of parameters.

The choices of parameters tested for use in the SGS curvature model heuristics are included in **Table 1**. The reconstructed estimate of the exact curvature from its modelled supergrid- and sub-grid-scale components – the approximation to Eq. (22) for insertion into Eqs. (15) and (16) – is done as

$$\kappa_{ij,k}^{\text{final}} = \kappa_{ij,k}^{\text{base}} + \kappa_{ij,k}^{\text{SGS}}. \quad (54)$$

The choices for $\kappa_{ij,k}^{\text{base}}$ and $\kappa_{ij,k}^{\text{SGS}}$, and the values of parameters for use in the model heuristics, are provided in **Table 1**. The resulting algorithm for the SGS curvature procedure is then simply a matter of sweeping through the mixed cells in the mesh, identifying if any of the five cases described above prevail, and computing $\kappa_{ij,k}^{\text{base}}$ and $\kappa_{ij,k}^{\text{SGS}}$ according to the prescriptions in **Table 1**.

3.5.3.2. SGS curvature Model 2: aggressive wrinkling. In the second SGS curvature model, more cases of curvature variation across filter scales are identified. For the non-curvature-limiting cases in Model 2, one consistent set of rules is formulated and used for determining the sign of the SGS curvature term, which determines whether the interface is locally smoothed (decrease in

effective curvature) or locally wrinkled (increase in effective curvature). While Cases 1–3 from Model 1 still apply in Model 2, Model 2 reveals various new possibilities for better computation of $\kappa_{ij,k}^{\text{SGS}}$.

Case 3: Inconsistency in variations between different curvature estimates.

The same criteria used in Model 1 for Case 3 (Eqs. (43)–(48)) are used here for identifying such variations. As compared to Model 1, Model 2 involves subdividing the case, with Eqs. (43)–(46) becoming the criteria for identifying Case 3a, and Eqs. (47) and (48) for Case 3b. This subdivision facilitates more targeted curvature limiting.

Case 6: Consistent difference between different filter length-scales.

If the differences between discretization-based and directly-filtered curvature estimates are large and consistent between the two coarse filter scales, it is likely that SGS curvature is important. Fulfillment of criteria

$$\left| \kappa_{ij,k}^{(\bar{C}(3\Delta))} \right| > \left| \kappa_{ij,k}^{(\bar{C}(2\Delta))} \right| + g_1 \quad (55)$$

and

$$\left| \bar{\kappa}_{ij,k}^{3\Delta} \right| > \left| \bar{\kappa}_{ij,k}^{2\Delta} \right| + g_2 \quad (56)$$

is used to identify Case 6m, while

$$\left| \kappa_{ij,k}^{(\bar{C}(3\Delta))} \right| + g_3 < \left| \kappa_{ij,k}^{(\bar{C}(2\Delta))} \right| \quad (57)$$

and

$$\left| \bar{\kappa}_{ij,k}^{3\Delta} \right| + g_4 < \left| \bar{\kappa}_{ij,k}^{2\Delta} \right| \quad (58)$$

is used to identify Case 6p.

Case 7: Outliers in direct-filtering curvatures.

If directly-filtered curvature estimate $\bar{\kappa}_{ij,k}^{3\Delta}$ is significantly different from all other discretization-based and directly-filtered curvatures generated using smaller filter lengths, it is the result of outliers from curvature data in the outer reaches of the 3Δ support affecting the estimate. Fulfillment of criterion

$$\left| \bar{\kappa}_{ij,k}^{3\Delta} \right| < j_1 \min \left(\kappa_{ij,k}^{(\bar{C}(\Delta))}, \kappa_{ij,k}^{(\bar{C}(2\Delta))}, \kappa_{ij,k}^{(\bar{C}(3\Delta))}, \bar{\kappa}_{ij,k}^{2\Delta}, \bar{\kappa}_{ij,k}^{3\Delta} \right) \quad (59)$$

is used to identify Case 7m, while

$$\left| \bar{\kappa}_{ij,k}^{3\Delta} \right| > j_2 \max \left(\kappa_{ij,k}^{(\bar{C}(\Delta))}, \kappa_{ij,k}^{(\bar{C}(2\Delta))}, \kappa_{ij,k}^{(\bar{C}(3\Delta))}, \bar{\kappa}_{ij,k}^{2\Delta}, \bar{\kappa}_{ij,k}^{3\Delta} \right) \quad (60)$$

is used to identify Case 7p.

Case 8: Curvature singularity.

A singularity in curvature results from interfacial phenomena such as filament rupture, and can lead to particularly high accelerations of the remnants. Discretization-based curvature schemes invariably smooth out such near-infinite local curvatures, affecting in turn interfacial transfer processes. This case is introduced to provide special support for the model to ameliorate curvature underestimation.

In this work, a singularity in the curvature is considered to coincide with massive underestimation of the curvature obtained via direct-filtering. The curvature singularity is identified when the following criteria are fulfilled:

$$\bar{\kappa}_{ij,k}^{2\Delta} < k_1 \kappa_{ij,k}^{(\bar{C}(\Delta))}, \quad (61)$$

$$\bar{\kappa}_{ij,k}^{2\Delta} < k_2 \kappa_{ij,k}^{(\bar{C}(2\Delta))}. \quad (62)$$

Case 9: No prescription.

Difference in signs between curvatures estimates at the smaller filter lengths

Table 1

Parameters for Model 1 heuristics on SGS curvature modelling procedure.

| Case | κ^{base} | κ^{SGS} | Model parameters |
|------|--|---|---|
| 1 | $\bar{\kappa}^{3\Delta}$ | $\kappa^{base} - \kappa^{\bar{C}(\Delta)}$ | $a = 0.2$ |
| 2 | $\kappa^{\bar{C}(\Delta)}$ | $f_1 \times \delta\kappa$, where $\delta\kappa = \begin{cases} \frac{1}{2} \kappa^{\bar{C}(2\Delta)} - \kappa^{\bar{C}(3\Delta)} & \text{if } d_2 < 0.2 \text{ and } d_1 > 2d_1 \\ \min \left(\begin{array}{l} \kappa^{\bar{C}(\Delta)} - \kappa^{\bar{C}(2\Delta)} , \\ \kappa^{\bar{C}(\Delta)} - \bar{\kappa}^{2\Delta} , \\ \kappa^{\bar{C}(2\Delta)} - \bar{\kappa}^{3\Delta} \end{array} \right) & \text{otherwise} \end{cases}$ | $f_1 = 0.2 \frac{d_1}{d_2}$ $f_1 = 0.05 \frac{d_1}{d_2}$ |
| 3 | $\text{sign}(\kappa^{\bar{C}(\Delta)}) \times \min \left(\begin{array}{l} \kappa^{\bar{C}(\Delta)}, \\ \kappa^{\bar{C}(2\Delta)}, \kappa^{\bar{C}(3\Delta)}, \\ \bar{\kappa}^{2\Delta}, \bar{\kappa}^{3\Delta} \end{array} \right)$ | $\kappa^{base} - \kappa^{\bar{C}(\Delta)}$ | $b_1 = 1.1$ $b_2 = 1.9$ |
| 4 | $0.5(\kappa^{\bar{C}(3\Delta)} + \bar{\kappa}^{3\Delta})$ | $\kappa^{base} - \kappa^{\bar{C}(\Delta)}$ | $c_1 > 2c_2$ $c_1 > 0.3$ |
| 5 | $0.5(\kappa^{\bar{C}(2\Delta)} + \bar{\kappa}^{2\Delta})$ | $\kappa^{base} - \kappa^{\bar{C}(\Delta)}$ | $d_3 > 4d_2$ $d_3 > 4d_1$ $d_1, d_2 < 0.2$ |

$$\kappa_{i,j,k}^{\bar{C}(\Delta)} \kappa_{i,j,k}^{\bar{C}(2\Delta)} < 0, \quad (63)$$

$$\bar{\kappa}_{i,j,k}^{2\Delta} \kappa_{i,j,k}^{\bar{C}(2\Delta)} < 0, \quad (64)$$

complicate efforts aimed at identifying consistent or inconsistent curvature variation. For now, no SGS modelling is enforced for such cases.

Case 10: Large change in discretization-based curvature at coarser filter lengths.

A large change in discretization-based curvature from the 3Δ filter to the 2Δ filter is indicative of non-uniform curvature within the filter support. This scenario is identified when the following criterion is fulfilled:

$$\left| \bar{\kappa}_{i,j,k}^{3\Delta} - \bar{\kappa}_{i,j,k}^{2\Delta} \right| / \left| \bar{\kappa}_{i,j,k}^{3\Delta} \right| < I_1 \left| \kappa_{i,j,k}^{\bar{C}(3\Delta)} - \kappa_{i,j,k}^{\bar{C}(2\Delta)} \right| / \left| \kappa_{i,j,k}^{\bar{C}(3\Delta)} \right|. \quad (65)$$

Case 10m identifies the case of Eq. (65) being fulfilled in conjunction with

$$\left| \kappa_{i,j,k}^{\bar{C}(2\Delta)} \right| < \left| \kappa_{i,j,k}^{\bar{C}(3\Delta)} \right|. \quad (66)$$

while

$$\left| \kappa_{i,j,k}^{\bar{C}(2\Delta)} \right| > \left| \kappa_{i,j,k}^{\bar{C}(3\Delta)} \right| \quad (67)$$

identifies Case 10p.

Case 11: Consistent large differences resulting from different filterings.

A more general case than Case 10 is when large differences between the discretization-based and direct-filtering curvatures take the form

$$\left| \kappa_{i,j,k}^{\bar{C}(2\Delta)} \right| / \left| \bar{\kappa}_{i,j,k}^{(2\Delta)} \right| < m_1 \quad (68)$$

and

$$\left| \kappa_{i,j,k}^{\bar{C}(3\Delta)} \right| / \left| \bar{\kappa}_{i,j,k}^{(3\Delta)} \right| < m_2 \quad (69)$$

for Case 11m, or

$$\left| \kappa_{i,j,k}^{\bar{C}(2\Delta)} \right| / \left| \bar{\kappa}_{i,j,k}^{(2\Delta)} \right| > m_3 \quad (70)$$

and

$$\left| \kappa_{i,j,k}^{\bar{C}(3\Delta)} \right| / \left| \bar{\kappa}_{i,j,k}^{(3\Delta)} \right| > m_4 \quad (71)$$

for Case 11p.

Signing procedure for smoothing versus wrinkling.

In Model 2, a signing procedure has been formulated to determine whether local smoothing or wrinkling is prescribed. This only applies to cases that do not feature explicit curvature limiting (in analogy to Model 1, the signing procedure would apply only to Case 2 of Model 1). In the signing procedure, the sign of the SGS curvature defaults to the sign for the regular curvature estimate $\kappa_{i,j,k}^{\bar{C}(\Delta)}$ in order to increase the local effective curvature (wrinkling). Specific rules are then defined to change the sign – usually to result in a decrease in effective curvature, through identification of inconsistencies in curvature variation between filter lengths. Table 2 features a listing of the different rules used for establishing the sign of κ^{SGS} . In Table 2, sign cases (i)–(v) are the default signing rules, while rules (vi)–(xiii) apply specifically to Case 11. The signs in Table 2 are then combined with Table 3 to prescribe SGS curvature.

Symmetry preservation.

The more extensive use of wrinkle-exacerbating options in Model 2 has the potential to introduce nonsymmetry into symmetrical problems. For interfacial turbulent flow problems involving interface wrinkling, the need for symmetry to be preserved over long time durations in flows is less important than for capillary flows, for instance. In the SGS curvature model, there is no explicit attempt to preserve the symmetry of κ^{SGS} distributions. Instead, symmetry preservation is promoted by controlling small errors in κ^{SGS} through a blocking procedure. A blocked SGS curvature can be computed as

$$\kappa^{SGSb} = s_1 \text{int} \left(\frac{\kappa^{SGS}}{s_1} \right), \quad (72)$$

where the blocking factor is

$$s_1 = 10^f, \quad (73)$$

with f determined by

$$f = \text{int}(\log_{10}(\kappa^{SGS})) + s_2. \quad (74)$$

3.5.4. Analogy with SGS stress modelling in LES

Drawing analogy with established methods for SGS modelling in LES of turbulent flow, the procedure presented here combines ideas of various modelling approaches. On the one hand, cases featuring SGS curvatures that are proportional to *differences between filtered estimates* makes the SGS curvature procedure resemble Smagorinsky-kernel models in LES. On the other hand for cases of inconsistent curvature variation, replacing the regular discretization curvature estimate with another filtered curvature estimate

Table 2
Rules in signing procedure for SGS curvatures in Model 2.

| | | Sign (modulo $\kappa^{\bar{C}(\Delta)}/ \kappa^{\bar{C}(\Delta)} $) | | | | | | | | | | | | | | | | | | | |
|----------------|---|--|----|----|----|----|----|----|----|----|----|----|----|-----|-----|-----|-----|-----|-----|-----|-----|
| Case | | 2m | 2m | 2p | 2p | 6m | 6m | 6p | 6p | 7m | 7m | 7p | 7p | 10m | 10m | 10p | 10p | 11m | 11m | 11p | 11p |
| Curvature sign | | + | - | + | - | + | - | + | - | + | - | + | - | + | - | + | - | + | - | + | - |
| Sign case | Rules | | | | | | | | | | | | | | | | | | | | |
| (0) | default | +1 | -1 | -1 | +1 | -1 | +1 | -1 | -1 | +1 | -1 | +1 | -1 | -1 | +1 | +1 | -1 | -1 | +1 | +1 | -1 |
| (i) | $ \kappa^{\bar{C}(2\Delta)} - \kappa^{\bar{C}(\Delta)} , \bar{\kappa}^{(2\Delta)} - \kappa^{\bar{C}(\Delta)} , \bar{\kappa}^{(3\Delta)} - \kappa^{\bar{C}(\Delta)} < 0.05 \kappa^{\bar{C}(\Delta)} $ | -1 | +1 | +1 | -1 | +1 | -1 | +1 | -1 | +1 | -1 | +1 | +1 | -1 | -1 | +1 | 0 | 0 | 0 | 0 | 0 |
| (ii) | $ \kappa^{\bar{C}(\Delta)} > \bar{\kappa}^{(2\Delta)} $ and $ \kappa^{\bar{C}(\Delta)} > \bar{\kappa}^{(3\Delta)} $ | -1 | +1 | +1 | -1 | +1 | -1 | +1 | -1 | +1 | -1 | +1 | +1 | -1 | -1 | +1 | +1 | -1 | -1 | -1 | -1 |
| (iii) | $ \bar{\kappa}^{(2\Delta)} < \kappa^{\bar{C}(\Delta)} $ and $ \bar{\kappa}^{(3\Delta)} > \kappa^{\bar{C}(\Delta)} $ | -1 | +1 | +1 | -1 | +1 | -1 | +1 | -1 | +1 | -1 | +1 | +1 | -1 | -1 | +1 | +1 | -1 | -1 | -1 | -1 |
| (iv) | $ \bar{\kappa}^{(2\Delta)} > \kappa^{\bar{C}(\Delta)} $ and $ \bar{\kappa}^{(3\Delta)} < \kappa^{\bar{C}(\Delta)} $ | -1 | +1 | +1 | -1 | +1 | -1 | +1 | -1 | +1 | -1 | +1 | +1 | -1 | -1 | +1 | +1 | -1 | -1 | -1 | -1 |
| (v) | $ \kappa^{\bar{C}(3\Delta)} - \bar{\kappa}^{(3\Delta)} / \bar{\kappa}^{(3\Delta)} > 0.25$ and $ \kappa^{\bar{C}(2\Delta)} - \bar{\kappa}^{(2\Delta)} / \bar{\kappa}^{(2\Delta)} < 0.05$ | -1 | +1 | +1 | -1 | +1 | -1 | +1 | -1 | +1 | -1 | +1 | +1 | -1 | -1 | +1 | | | | | |
| (vi) | $ \kappa^{\bar{C}(2\Delta)}/\bar{\kappa}^{(2\Delta)} < 0.2$ and $ \kappa^{\bar{C}(3\Delta)}/\bar{\kappa}^{(3\Delta)} < 0.1$ | | | | | | | | | | | | | | | | | -1 | +1 | | |
| (vii) | $ \kappa^{\bar{C}(2\Delta)} > \kappa^{\bar{C}(3\Delta)} $ and $ \bar{\kappa}^{(2\Delta)} < \bar{\kappa}^{(3\Delta)} $ | | | | | | | | | | | | | | | | | +1 | | | |
| (viii) | $ \kappa^{\bar{C}(2\Delta)} < \kappa^{\bar{C}(3\Delta)} $ and $ \bar{\kappa}^{(2\Delta)} > \bar{\kappa}^{(3\Delta)} $ | | | | | | | | | | | | | | | | | +1 | | | |
| (ix) | $ \kappa^{\bar{C}(3\Delta)}/\bar{\kappa}^{(3\Delta)} < 0.2$ | | | | | | | | | | | | | | | | | +1 | -1 | | |
| (x) | $ \kappa^{\bar{C}(\Delta)}/\kappa^{\bar{C}(2\Delta)} < 0.5$ | | | | | | | | | | | | | | | | | | | -1 | +1 |
| (xi) | $ \kappa^{\bar{C}(2\Delta)} > \kappa^{\bar{C}(3\Delta)} $ and $ \kappa^{\bar{C}(\Delta)} < \kappa^{\bar{C}(2\Delta)} $ | | | | | | | | | | | | | | | | | | +1 | -1 | |
| (xii) | $ \kappa^{\bar{C}(2\Delta)} > \kappa^{\bar{C}(3\Delta)} $ | | | | | | | | | | | | | | | | | | | -1 | +1 |
| (xiii) | $ \kappa^{\bar{C}(\Delta)} > \kappa^{\bar{C}(2\Delta)} $ and $ \kappa^{\bar{C}(2\Delta)} < \kappa^{\bar{C}(3\Delta)} $ | | | | | | | | | | | | | | | | | | | -1 | +1 |

is *curvature limiting*, and resembles the effect of flux-limiting in momentum advection schemes in Monotone-Integrated Large Eddy Simulation (MILES) [3]. The methodology indeed introduces a physically sound model for energy transfer between interfacial length scales in the vicinity of the filter scales. With the successful implementation of the SGS curvature model into the TransAT software [51], future research is aiming to ascertain to what extent the vast array of SGS stress modelling procedures from LES can be applied to SGS curvature closure in the LEIS of practical problems, e.g. in sectors such as thermal-hydraulics of nuclear reactors, oil and gas, and environmental/coastal engineering.

4. SGS curvature tests

While static equilibrium is the most common test for surface tension modelling, it involves spheres or circles with constant curvature. Sphere/circle tests are clearly inadequate as tests for important flow scenarios involving sharp spatial variation in curvature, e.g. jets, fragmentation/coalescence events. Additional numerical experiments are therefore presented here to address the utility of curvature schemes in such scenarios.

The performance of the SGS curvature model is assessed by comparing the L_1 errors of the procedure to those based on regular discretization:

$$L_1 = \frac{\sum \tilde{\delta} |\kappa^{final} - \kappa^{exact}| \delta V}{\sum \tilde{\delta} \delta V}, \quad (75)$$

where $\tilde{\delta}$ is the local approximation to the delta function, and δV is the volume of the mesh cell (filter volume). This error, and in particular the Kronecker- δ -dependence, has been introduced to reflect the weighting of individual mixed-cell curvature estimates within the CSF surface force estimate (Eq. (18)); $\tilde{\delta}$ is estimated from ∇C off the local mesh.

4.1. 3D cosine wave

The 3D cosine wave test (Liovic *et al.* [27]) features a curvature distribution that is not spatially uniform and changes relative to mesh size. For any (x, y) coordinate, the cosine wave is initialized as

$$z_{wave} = A - B \cos\left(\frac{2n\pi w}{L}\right), \quad (76)$$

where w is the projection of the 2D coordinate vector $x\mathbf{i} + y\mathbf{j}$ onto the propagation direction $\mathbf{p} = \mathbf{i} + \mathbf{j}$. In the current test, we use $L = 8$, $A = 4$, $B = 1$ and $n = 4$; the resultant interface shape within a $8 \times 8 \times 8$ solution domain is shown in Fig. 3a. The exact (non-normalized) unit interface normal corresponding to a 2D cosine wave is easily extracted by setting $h = z$, i.e. $\mathbf{n} = (h_x, h_y, h_z) = (z_x, z_y, 1)$. The exact curvature corresponding to a 2D cosine wave propagated in the direction of increasing w is

$$\kappa^{exact} = -\frac{z''}{(1 + (z')^2)^{3/2}}. \quad (77)$$

The wave features high-curvature peaks and troughs that remain beyond the reach of curvature discretization schemes, and for which SGS modelling support is particularly desirable. The setup has low-curvature regions as well, such that discretization should adequately resolve and SGS closure should locally be negligible.

4.2. 3D Gaussian wave

The Gaussian wave test introduced here is a 3D variant of the 2D Gaussian wave test introduced for interface normal testing in [6], and features abruptly changing interface normals and curvature. For any (x, y) coordinate, the Gaussian wave is initialized as

$$z_{wave} = A + B \exp(C(w - D)^2). \quad (78)$$

As in the previous test, use is made of the projection w of the 2D coordinate vector $x\mathbf{i} + y\mathbf{j}$ onto the propagation direction $\mathbf{p} = \mathbf{i} + \mathbf{j}$. In the current test, we use $A = 1/10$, $B = 3/4$, $C = -25$ and $D = 1$, as in [6]; the resultant interface shape initialized within a $2 \times 2 \times 2$ solution domain is shown in Fig. 3b. (Note the similarity in 2D waveforms with the bubble interface in the Ultrasound Contrast Agent microbubble volume oscillation in [8,47].)

4.3. Comparisons

Table 4 shows the L_1 errors obtained for the 3D cosine wave test with and without SGS curvature modelling support. It shows that over 30% reduction in curvature error can be achieved in some cases using Model 1. This figure can be improved on with more work, with Model 2 showing a substantial improvement even over Model 1. Unfortunately those gains in Model 2 are not sustainable over a broad mesh resolution range.

Table 3

Parameters for Model 2 heuristics on SGS curvature modelling procedure, where the SGS curvature is computed as $\kappa^{SGS} = \text{sign} \times \text{factor} \times \text{magnitude}$.

| Case | Factor | Magnitude | Model parameters |
|------|---|--|---|
| 2 | $1.5 \frac{ \kappa^{\bar{C}(2\Delta)} - \kappa^{\bar{C}(3\Delta)} }{0.5(\kappa^{\bar{C}(2\Delta)} + \kappa^{\bar{C}(3\Delta)})}$ | $\min \left(\begin{array}{l} \kappa^{\bar{C}(\Delta)} - \kappa^{\bar{C}(2\Delta)} , \\ \kappa^{\bar{C}(\Delta)} - \kappa^{2\Delta} , \\ \kappa^{\bar{C}(2\Delta)} - \kappa^{2\Delta} \end{array} \right)$ | |
| 6 | $1.0 \frac{ \kappa^{\bar{C}(2\Delta)} - \kappa^{\bar{C}(3\Delta)} }{0.5(\kappa^{\bar{C}(2\Delta)} + \kappa^{\bar{C}(3\Delta)})}$ | $\min \left(\begin{array}{l} \kappa^{\bar{C}(\Delta)} - \kappa^{\bar{C}(2\Delta)} , \\ \kappa^{\bar{C}(\Delta)} - \kappa^{2\Delta} , \\ \kappa^{\bar{C}(2\Delta)} - \kappa^{2\Delta} \end{array} \right)$ | $g_1 = 0.5(\kappa^{2\Delta} + \kappa^{3\Delta})$ $g_2 = g_1$ $g_3 = g_1$ $g_4 = g_1$ |
| 7 | $1.0 \frac{ \kappa^{\bar{C}(2\Delta)} - \kappa^{\bar{C}(3\Delta)} }{0.5(\kappa^{\bar{C}(2\Delta)} + \kappa^{\bar{C}(3\Delta)})}$ | $ \kappa^{\bar{C}(2\Delta)} - \kappa^{3\Delta} $ | $j_1 = 0.9$ $j_2 = 1.1$ |
| 8 | | | $k_1 = 0.1$ $k_2 = 0.1$ |
| 10 | $0.25 \frac{ \kappa^{\bar{C}(2\Delta)} - \kappa^{\bar{C}(3\Delta)} }{0.5(\kappa^{\bar{C}(2\Delta)} + \kappa^{\bar{C}(3\Delta)})}$ | $ \kappa^{\bar{C}(2\Delta)} - \kappa^{3\Delta} $ | $l_1 = 0.2$ |
| 11m | $0.5 \frac{ \kappa^{\bar{C}(2\Delta)} - \kappa^{\bar{C}(3\Delta)} }{0.5(\kappa^{\bar{C}(2\Delta)} + \kappa^{\bar{C}(3\Delta)})}$ | $ \kappa^{\bar{C}(2\Delta)} - \kappa^{3\Delta} $ | $m_1 = 0.67$ $m_2 = 0.67$ |
| 11p | $1.0 \frac{ \kappa^{\bar{C}(2\Delta)} - \kappa^{\bar{C}(3\Delta)} }{0.5(\kappa^{\bar{C}(2\Delta)} + \kappa^{\bar{C}(3\Delta)})}$ | $ \kappa^{\bar{C}(2\Delta)} - \kappa^{3\Delta} $ | $m_3 = 1.5$ $m_4 = 1.5$ |

Table 5 shows the L_1 errors obtained for the 3D Gaussian wave test with and without SGS curvature modelling support. It again shows that 30 percent reductions in curvature error can be achieved using Model 1. The results show that the modelling procedure is capable of detecting wrinkling, and to some extent compensating for the under-resolution of discretization. Given tuning of Model 2 was based on the 3D cosine wave test, it is not necessarily surprising that Model 2 did not perform as well for the Gaussian wave test. Improvements to the aggressive wrinkling methodology behind Model 2 may involve more tuning of model settings on a wider range of static curvature tests.

5. Static drop tests

The static drop is a classical test of surface tension schemes, assessing the predictive capability of the schemes to reproduce the pressure variation prescribed by the Young–Laplace law

$$\Delta P = \gamma \left(\frac{1}{R_1} + \frac{1}{R_2} \right), \quad (79)$$

and to preserve static equilibrium. Parasitic currents induced by surface tension discretization scheme errors can prevent the bubble reaching static equilibrium.

The current study involves a static drop test, featuring the balanced-force MFVOF-3D flow solver [27]. Use of this balanced-force option is particularly useful, because the solver has been verified to preserve static equilibrium to machine-zero when the exact curvature of a circular or spherical is imposed. The static drop test here compares the regular height function curvature scheme with the height function scheme supported by SGS curvature modelling contributions. Simplifying the analysis using a 2D problem setup, a 30×30 mesh is used to span a $0.075 \text{ m} \times 0.075 \text{ m}$ flow domain, in which a drop of radius 0.021 m is centred. Following examples used in the original CSF work of Brackbill et al. [5], bulk properties of ethanol and air are used ($\rho_l = 797.88 \text{ kg/m}^3$, $\mu_l = 1.2 \times 10^{-3} \text{ Pa s}$, $\rho_g = 1.18 \text{ kg/m}^3$, $\mu_g = 1.0 \times 10^{-5} \text{ Pa s}$), and surface tension $\gamma = 2.36 \times 10^{-2} \text{ N/m}$. In the first instance, viscosity is neglected in order to remove its dissipative effect.

The simulations do well in all cases in reproducing the pressure drop prescribed by Eq. (79). The top row of Fig. 4 shows the total kinetic energy [12]

$$TKE = \frac{1}{2} \sum_{ncells} \left(\sum_k C_k \rho_k \right) \mathbf{u}_c \cdot \mathbf{u}_c \delta x \delta y \delta z \quad (80)$$

generated by the flow solver for the static drop problem in the case of inviscid flow. The flow solver featuring the SGS surface tension model results in a 35 percent decrease in average kinetic energy as compared to the result using only height function curvature discretization with SGS support. A more usual means of comparing surface tension schemes for this problem is to compare maxima in velocity. The middle row of Fig. 4 shows the improvement achieved by using the SGS model appears more pronounced when u_{max} is plotted. The difference in the extent of the improvement shows the action of the curvature-limiting cases of the SGS modelling to keep the largest error modes under control. The incremental wrinkling/smoothing cases are not active for this constant-curvature scenario, hence compensation for error over the entire interface support is not performed anywhere near as dramatically as it could be.

The bottom row of Fig. 4 shows the results when viscosity is activated. The damping effect of viscosity is far more dramatic for the case without SGS modelling support, which suffers from maximum parasitic current velocities about twice as large as the case using the SGS model. Again, the dominance of the constant-curvature scenario means that the no-SGS-model result converges to the SGS model result in a finite period of time. It is apparent that the current SGS model implementation is impressive in reducing parasitic currents without totally eliminating them. More aggressive settings in the SGS model may be useful for reducing parasitic currents to minimal intensity, and will be investigated in further work.

6. Drop oscillation tests

The heuristic nature of the current SGS model for curvature makes static curvature tests insufficient for assessing SGS surface tension modelling. Drop tests are required to ensure that the heuristics choices and model parameters are generally applicable across a wide spectrum of interface configurations.

The drop oscillation test considered here is the 2D square drop test, first introduced by Brackbill et al. [5], whereby a square drop of ethanol ($\rho_l = 797.88 \text{ kg/m}^3$, $\mu_l = 1.2 \times 10^{-3} \text{ Pa s}$) of side length $D = 0.041 \text{ m}$ is centered in a domain of size $0.075 \text{ m} \times 0.075 \text{ m}$ is

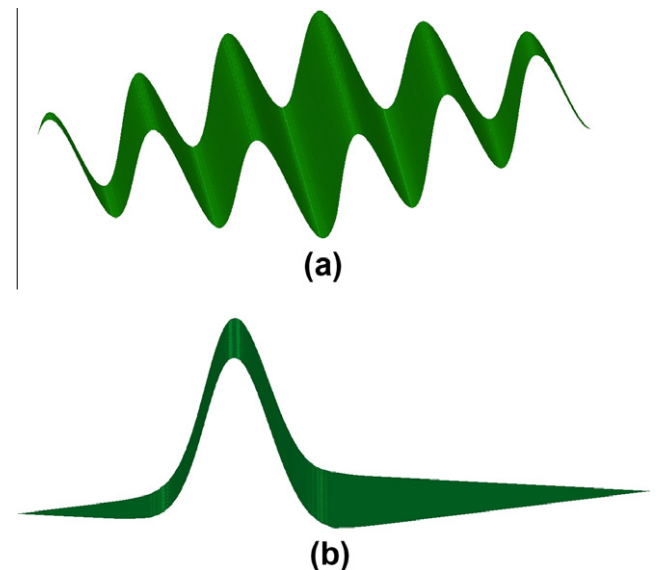


Fig. 3. Initialization of interface shape for (a) 3D cosine wave problem; (b) 3D Gaussian wave problem.

surrounded by air ($\rho_g = 1.18 \text{ kg/m}^3$, $\mu_g = 1.0 \times 10^{-5} \text{ Pa s}$). The surface tension in this case is $\gamma = 2.36 \times 10^{-2} \text{ N/m}$. The period of drop oscillation is approximated by the linear theory

$$T_{\text{linear}} = \frac{2\pi R_{\text{eq}}^3 (\rho_l + \rho_g)}{\gamma(n^3 - n)}, \quad (81)$$

where the $n = 2$ perturbation is considered, and the equivalent radius of the square drop is

$$R_{\text{eq}} = \frac{D}{\sqrt{\pi}}. \quad (82)$$

For the current configuration, the period is $T_{\text{linear}} = 0.42 \text{ s}$. Full transformation of the initially square drop to a straight-edged diamond-shaped drop at $T_{\text{linear}}/2$ was found by Brackbill et al. [5] and Vincent et al. [52] to validate surface tension modelling. (In [5,52], the authors show plots at $t = 0.2 \text{ s}$ – slightly before $T_{\text{linear}}/2$.) For direct comparison with [5], the 30×30 mesh used in that work is also used here. The solution algorithm options here are also consistent with the flow solver used in [5] – specifically the use of the CSF scheme in preference to the SSF scheme, and the use of the velocity formulation of the Navier-Stokes equations as the basis for discretization. A timestep size of $\delta t = 1.5 \times 10^{-5} \text{ s}$ is used to ensure adequate time-resolution of flow reversal in the oscillation.

More than simply featuring non-constant curvature, the square drop oscillation test initially features singularities in the curvature at the corners of the square, bounding edges of initially zero curvature. To assess the significance of these abrupt changes in interface wrinkling, the test is firstly performed using the flow solver featuring a standard fully kernel-based CSF scheme [39]. Snapshots using this surface tension scheme are shown in the leftmost column 1 of Fig. 5. The $t = 0.22 \text{ s}$ snapshot features straight edges at the $\pi/4$, $3\pi/4$, $5\pi/4$ and $7\pi/4$ azimuthal locations and (near-)maximum extent parallel to the Cartesian axis directions ($\pi/2$, π , $3\pi/2$ and 2π). These features resemble the diamond-shaped drop snapshots used in [5,52] to ascertain recovery of the $T_{\text{linear}}/2$ from linear theory. As such, the kernel-based CSF result at $t = 0.22 \text{ s}$ is used in this test as the estimate to the $T_{\text{linear}}/2$ result, against which surface tension modelling features SGS curvatures are compared.

For first comparison with the kernel-based CSF result in column 1, column 2 presents the result achieved using the height function method for curvature estimation, without any SGS support. The result at $t = 0.22 \text{ s}$ using regular height function curvature estimates is worse than the result from the kernel-based CSF, with the diamond edges at the $\pi/4$, $3\pi/4$, $5\pi/4$ and $7\pi/4$ azimuthal locations being significantly curved rather than straight. The period is overestimated by at least $0.1 T_{\text{linear}}$; this is regardless of the well known fact that height function-based curvature estimation is generally superior to other methods. The reason for this poor performance is because the “45-degree” problem [27] coincides with the azimuthal location (relative to the drop centre) of the initially discontinuous curvature distribution. In this case, poor initial estimates of curvature near the initial corners of the square delays the develop-

ment of oscillations. The results in column 2 of Fig. 5 clearly demonstrate a notable shortcoming in the surface tension module relying solely on height function curvatures.

The value of SGS curvature modelling for improving interfacial flow simulations is shown in column 3 of Fig. 5. In this case, SGS curvature Model 1 is effective in regularizing the receding $\pi/4$, $3\pi/4$, $5\pi/4$ and $7\pi/4$ interfaces at $t = 0.22 \text{ s}$. The straightness of these edges at $t = 0.22 \text{ s}$ from using Model 1 is a clear improvement on sole use of the height function curvature discretization scheme without SGS support, and makes the results comparable to the convolution case and other documented results. Unfortunately Model 1 seeds nonsymmetry into the surface tension-dominated interfacial flow, such that the symmetry losses at $t = 2 \text{ s}$ are visible. SGS curvature Model 2, however, seems to do a far better job in preserving symmetry to $t = 2 \text{ s}$ and beyond. Model 2 also does well at creating and exacerbating high-curvature regions, as indicated by the narrowness of the new corners in the diamond shape. More tuning of Model 2 is expected to be useful in allowing the analytical drop oscillation period to be better reproduced, with the receding $\pi/4$, $3\pi/4$, $5\pi/4$ and $7\pi/4$ interfaces at $t = 0.22 \text{ s}$ not being as straight as achieved using Model 1 for SGS curvature or convolution for surface tension discretization. Nonsymmetries in drop oscillation simulations may also be introduced outside of the surface tension modelling, such as in direction-split VOF modules. In such cases, the robustness of the SGS modelling is quite reliant on the blocking step in Eq. (72) to round off small nonsymmetries.

7. Unresolved surface tension in wave-breaking surf zones

The previous section assessed the SGS curvature model within the framework of the numerical discretization schemes for curvature (e.g. [5,7,12,27]), without showing how the LEIS of turbulent multi-material flows is improved. To demonstrate now the performance of the new SGS curvature model as an LEIS closure model (Eq. (16)), the problem of wave breaking is considered. Fig. 6 is useful in identifying the various phenomena taking place in the wave breaking process as the origin of a broadband spectrum of interfacial length-scales. The figure also shows the need for accurate surface tension modelling for capturing interface wrinkling, microbreaking, bubble and drop formation and their instability-based precursors. In the current study, we consider the spilling breaker scenario investigated experimentally by Ting and Kirby [48] (henceforth referred to as TK96) and numerically by Lakehal and Liovic [30]. A *a priori* analysis of SGS closure terms in [26,30] focused on ascertaining the imperative for SGS closure for unresolved surface tension by comparing the magnitude of the unresolved surface tension term with the SGS stress term (Eq. (17)). In the current study, we instead use the SGS curvature model to determine the extent to which its use contributes to the unresolved surface tension SGS term, using an *a posteriori* analysis.

The *a posteriori* analysis is based on evaluating a flow sample of the surf zone interface topology from the 2D TK96 simulation [30], and generate numerical estimates for the resolved curvature and interface normal throughout the interface support, then apply explicit filtering to those resolved-mesh distributions. The filtering applied to the unfiltered surface tension in Eq. (24) can similarly be applied to the same term in Eq. (16) as

$$\epsilon_\gamma = \gamma(\bar{\kappa} + \kappa^{\text{SGS}})(\bar{\mathbf{n}} + \hat{\mathbf{n}}^{\text{SGS}})\delta - \gamma(\bar{\kappa} + \kappa^{\text{SGS}})(\bar{\mathbf{n}} + \hat{\mathbf{n}}^{\text{SGS}})\delta, \quad (83)$$

where a standard tophat filter is applied. Based on the observation that $|\kappa^{\text{SGS}}| \gg |\hat{\kappa}^{\text{SGS}}|$ and $|\kappa^{\text{SGS}}/\bar{\kappa}| \gg |\hat{\kappa}^{\text{SGS}}/\bar{\kappa}|$ overwhelmingly prevail, closure is approached ($\epsilon_\gamma \rightarrow 0$) if the spatial distribution of κ^{SGS} is realistically reconstructed throughout the interface support. Poor

Table 4

Errors in curvature estimation for a 3D cosine wave, using the height function-based curvature scheme without SGS curvature closure, and with SGS curvature evaluated from the new SGS curvature modelling procedure included.

| | HF curvature only | HF curvature + SGS curvature Model 1 | HF curvature + SGS curvature Model 2 |
|-----------------------------|-----------------------|--------------------------------------|--------------------------------------|
| $32 \times 32 \times 32$ | 4.30×10^{-1} | 3.65×10^{-1} | 3.07×10^{-1} |
| $64 \times 64 \times 64$ | 7.15×10^{-1} | 5.01×10^{-1} | 6.25×10^{-1} |
| $128 \times 128 \times 128$ | 8.54×10^{-2} | 7.79×10^{-2} | 8.22×10^{-2} |

Table 5

Errors in curvature estimation for a 3D Gaussian wave, using the height function-based curvature scheme without SGS curvature closure, and with SGS curvature evaluated from the new SGS curvature modelling procedure included.

| | HF curvature only | HF curvature + SGS curvature | HF curvature + SGS curvature |
|-----------------------------|-----------------------|------------------------------|------------------------------|
| | | Model 1 | Model 2 |
| $32 \times 32 \times 32$ | 1.05×10^0 | 8.61×10^{-1} | 1.01×10^0 |
| $64 \times 64 \times 64$ | 6.73×10^{-1} | 4.69×10^{-1} | 6.44×10^{-1} |
| $128 \times 128 \times 128$ | 1.23×10^{-1} | 1.13×10^{-1} | 1.27×10^{-1} |

capturing of the true nonuniformity in the κ^{SGS} distribution is clearly visible in contour plots because of the smearing nature of the tophat filter.

The top panel of Fig. 7 shows the interface region in the surf zone following a wave breaking event; the black lines show the 0.05, 0.5 and 0.95 isocontours in the color function \bar{C} , and the waves in the simulated flow propagate and break from left to right. The combined action of the surface tension scheme support and the tophat filter stencil broaden the colored interface region by up to four mesh cells from a sharp interface location. The left side of the contiguous free surface in the top panel of Fig. 7 shows the

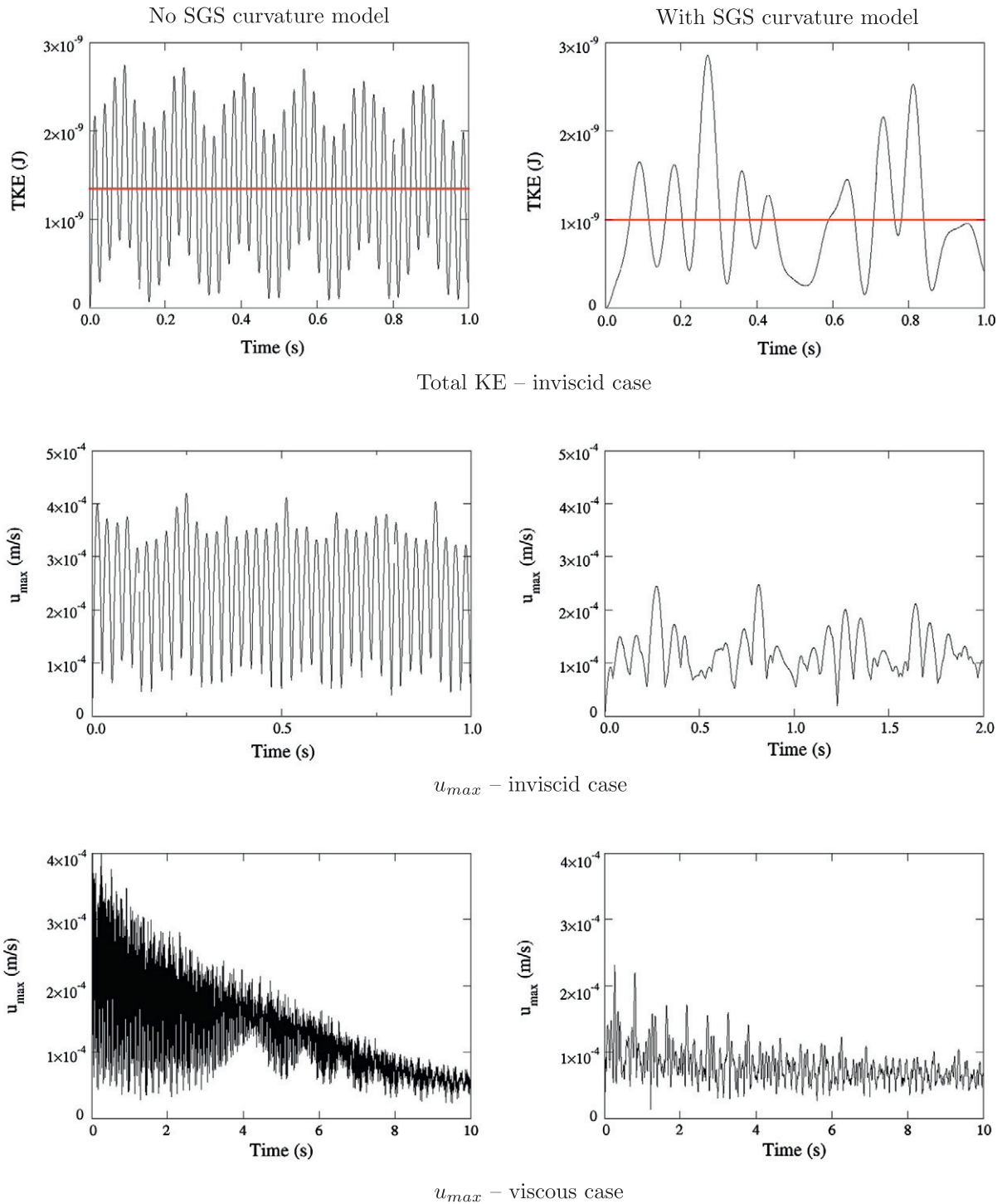


Fig. 4. Results for the 2D static drop test, with and without the SGS curvature model in support of the regular height function curvature discretization scheme.

free surface to be compact seaward of the breaker. In contrast, the relatively diffuse nature of the interface topology shoreward of the breaker is indicative of fragmentation, in the form of entrained bubbles and ejected spray droplets. The lack of three distinct line isocontours above the free surface indicates that the sea spray droplets as represented on the 2D mesh are (for the most part) sub-grid scale, such that the real size of upwardly ejected droplets is far smaller than that in the colored regions in the upper part of the top panel. [The 2D predictions of spray droplets also differ from the 3D real nature, if simulated 2D solutions are considered to be long-shore-averaged representations of 3D flow phenomena.]

The rows below the top panel of Fig. 7 zoom in on different sub-zones of the region shown in the top panel, and show magnitudes of the unresolved surface tension closure term (z -component ϵ_{yz}) when no SGS support is provided (right column), and when the new SGS curvature model is used (left column). While the distributions resulting from using the SGS curvature model visually do not differ in interface support width from those obtained without the model, the overall lower magnitudes of the closure term achieved with the model are obvious. Table 6 confirms the SGS curvature model to be quite effective in bridging some of the closure gap, with error norms nearly half the magnitude of ϵ_{yz} . The TK96 simulation data set from [30] is based on one mesh resolution, so a more thorough *a posteriori* analysis that better delineates discretization error and SGS model contributions should probably be performed. In any case, the analysis performed here does show the proposed SGS curvature model to be effective without tuning.

8. 3D bubble bursting at a free surface

The bursting of a bubble at a free surface is an important problem in nature, and in various conventional and novel technologies. Sea spray drops ejected by bursting bubbles in oceans (especially in surf zones) are important for fog and cloud formation. Fig. 6 illustrates the manner in which air entrainment caused by coastal wave breaking results in surf zone aeration through bubble entrainment [54,30]. Splash drops in pyrometallurgical smelters are important for the downward transport of heat from post-combustion in the freeboard space into the bath. Experimental investigations of a single bubble bursting at a free surface date back to Kientzler et al. [20]. Examples of simulation techniques range from boundary-integral method [4] to multi-material DNS using markers for interface tracking [10]. Günther et al. [13] summarize the distinction between drops formed from jet break-up, and early drops formed by film rupture. In bypassing film drainage and rupture, computational studies conducted hitherto decouple bubble rise from bubble bursting. The greater net surface area associated with film drops has obvious consequences for transfer processes between the gas and liquid phases. It is hence desirable that the simulation technique employed can naturally capture bubble-cap film break-up together with all other relevant interface kinematic events, including bubble rise, ejection of jet drops and individual film drop trajectories. This test case is the final problem considered in this paper here as part of the SGS surface tension model validation within the LEIS framework.

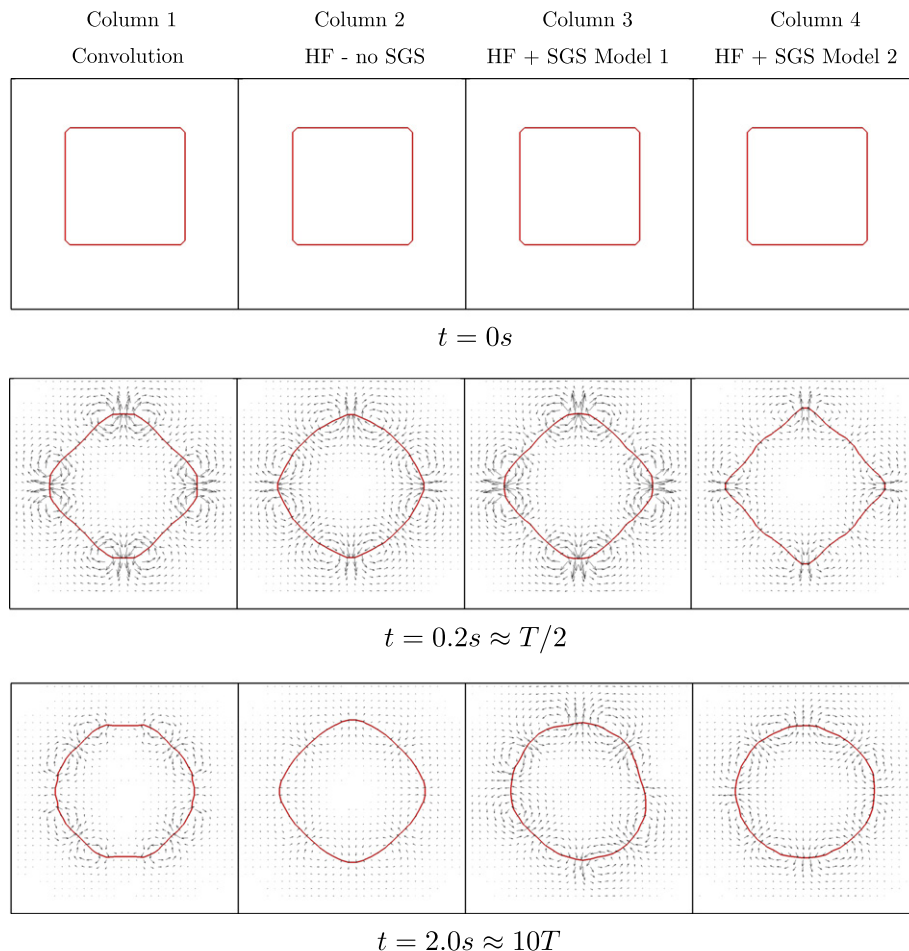


Fig. 5. Results for the 2D square drop oscillation test, using various discretization schemes and the two variants of the SGS curvature model.

8.1. Bubble rise and bursting as a Large Eddy and Interface Simulation

Using the local radius of curvature as an indicator of interfacial length scale, the case of well-resolved laminar bubble rise features an interfacial length-scale spectrum that essentially saturates at a length scale coarser than the filter scale. In such cases, DNS of the multi-liquid interfacial flow has been achieved. From experimental studies of bubble bursting, it is known that CFD of *mm*-bubble bursting will not achieve DNS of the interfacial flow. This is because the mean diameters of film drops are in the range of $10\ \mu\text{m}$ [41], and because film thicknesses are smaller than film drop diameters and even sub-micron [42].

In the bubble bursting event, it is useful to identify three key interfacial phenomena: (i) bubble cap liquid filamentation due to film drainage hydrodynamics; (ii) film rupture; and (iii) consolidation of post-rupture film liquid into drops. Phenomena (i) and (iii) feature identical physical forms across length scales all the way down to the micron scale (e.g. squeezing flow for films; re-orientation to minimum-energy configurations for drops) – hence lending themselves to occurring in a similar manner across the relevant *mm/μm* part of the length scale spectrum. Film rupture phenomenon (ii) occurs as a result of hydrodynamic drainage to the extent that opposing interfaces in the film are brought close enough together, such that attractive van der Waals forces between the interfaces trigger the bubble-coalescence event. (More discussion of short-range interfacial interactions in relation to VOF-based simulation of drop/bubble coalescence is provided in [14].) Such interfacial interactions occur on a *nm*-scale, meaning that any individual rupture event and the preceding film drainage at *nm*-scale film thicknesses is, in principle, a phenomenon that is scale-separated from the *mm/μm*-scale phenomena in the overall bubble bursting event. In reality, propagation of wave disturbances along interfaces can cause film rupture on time-scales faster than predicted in lubrication theory-based film drainage descriptions. Wave disturbances initiated by interfacial instabilities or interface-turbulence interaction are still hydrodynamic in nature and occur in a similar manner in the *mm/μm* part of the interfacial length scale spectrum.

A final point on bubble bursting as a problem for LEIS is that there are notable procedural differences in the analysis of flow field data (experimental or model) from the bursting flow as compared to bubble rise. In the case of bubble rise, the motion is rela-

tively reproducible in terminal velocity and aspect ratio, and generally features low variability from one experiment to the other. As such, single experiments and/or simulations of bubble rise flow are usually considered adequate for quantitative analysis. In contrast, bubble bursting is inherently a statistically variable flow, with averaging over large ensembles recommended for reliable statistical analysis. The slightest nonsymmetry in bubble rise will typically be exacerbated in the bubble bursting event as non-symmetries in bubble cap film breakup and film drop ejection. To reinforce this, Spiel [41] noted that the bursting bubble may eject film drops over only part of the film's periphery. In contrast, jet formation and jet drop ejection is experimentally observed to be essentially symmetrical in vertical planes of symmetry through the centroid of the bubble. Consideration of ensembles of simulations makes LEIS a more feasible tool than DNS for the analysis of interfacial flows featuring significant statistical variability.

8.2. Problem setup

Bubble bursting simulation is performed here as a continuation of the bubble rise investigation performed by Liovic et al. [27]. In that study inspired by the investigation of Sussman and Ohta [43], the base problem setup of Hnat and Buckmeister [17] was selected in which a $d_e = 12.15\ \text{mm}$ bubble of air rises through mineral oil ($\rho_G = 1.2\ \text{kg/m}^3$, $\mu_G = 1.8 \times 10^{-5}\ \text{Pa s}$, $\rho_L = 876\ \text{kg/m}^3$, $\mu_L = 1.18 \times 10^{-1}\ \text{Pa s}$, $\gamma = 32.2 \times 10^{-2}\ \text{N/m}$.) Bubbles of 12 mm diameter were selected instead of the 3 mm bubbles in order to compare to the Spiel [41] data, which suggest a transition in bubble bursting in the 3 – 4 mm-diameter range in air/tap-water systems. Spiel [41] hypothesized that the bursting of bubbles smaller than 3 – 4 mm in diameter featured film *roll-up* into a toroidal ring that gathers mass as it advances towards the edge, while bubbles larger than 3 – 4 mm in diameter feature *film disintegration*, during which the films fracture and drops are thrown out simultaneously over the entire film surface. The implied prospect for greater symmetry of film drop ejections in the larger bubble case motivated first consideration of the 12 mm bubble for studying bursting.

Similar to the setup in [27], flow initialization of the bubble bursting problem was achieved by mirroring the first *xy*-quadrant flow field into the remaining quadrants. A free surface between the bulk liquid and gas phases was then initialized at

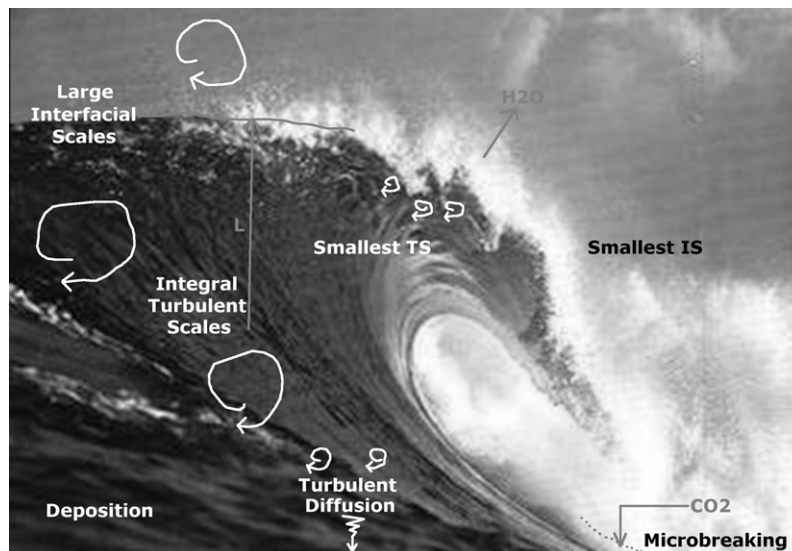


Fig. 6. Coastal wave breaking, featuring the early stages of air entrainment by a plunging breaker, as well as other phenomenology including bubble bursting as an integral component in maintaining global mass balance of air in the surf zone.

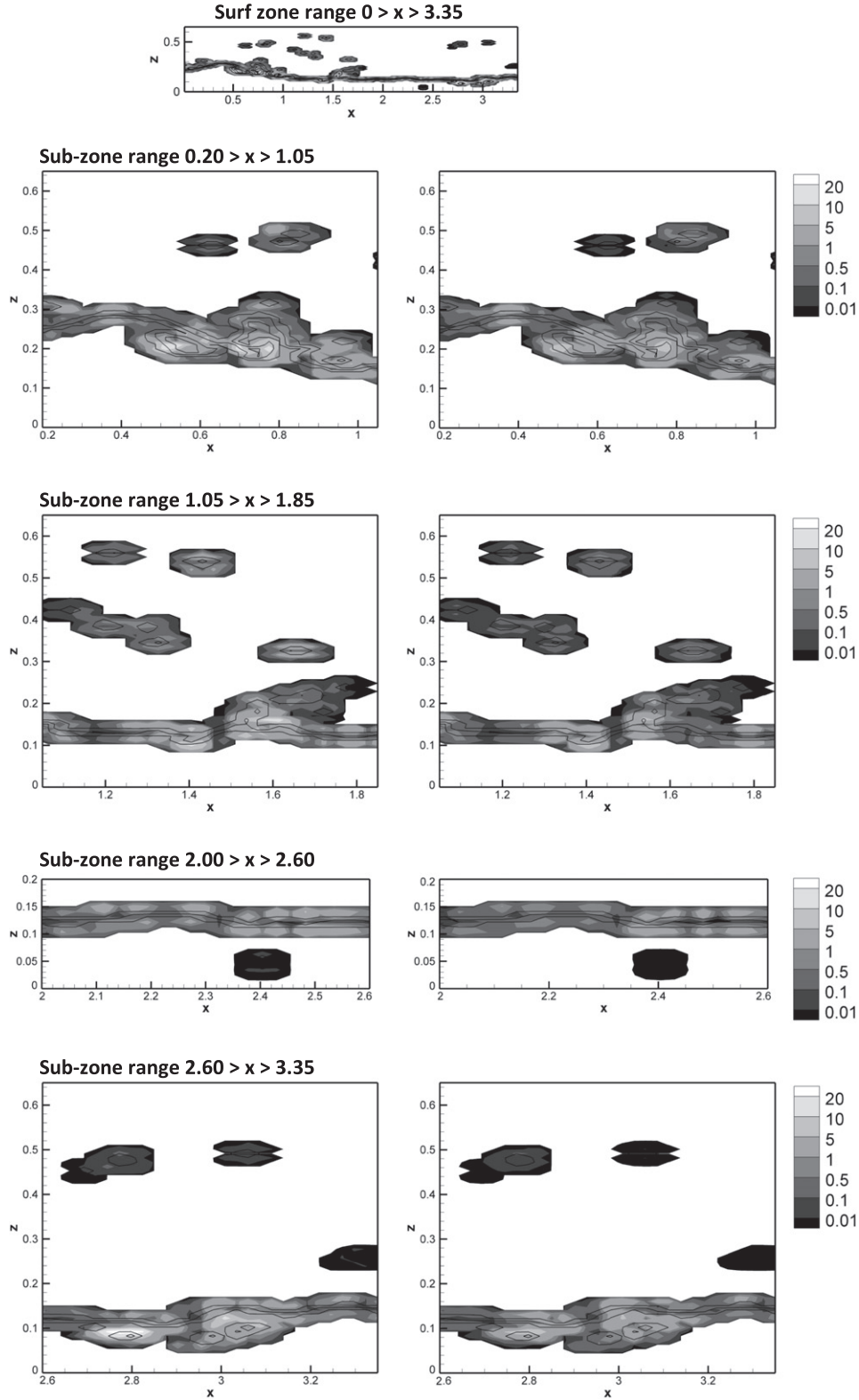


Fig. 7. Spatial distributions of under-resolved surface tension term ϵ_γ for a snapshot from the validated Liovic/Lakehal [30] simulation of the TK96 experiment [48], where the local curvature estimate κ used in Eq. (16) is a combination of the resolved (numerical) and unresolved (SGS model) contribution: (a, shown on left) ϵ_{γ_z} without use of κ^{SGS} , i.e. filter based on $\kappa = \bar{\kappa}$; (b, shown in right) ϵ_{γ_z} with use of κ^{SGS} , i.e. filter based on $\kappa = \bar{\kappa} + \kappa^{SGS}$. [Coordinates x and z are in metres.]

$5d_e$ above the location of the bubble, and the simulation restarted on a $96 \times 96 \times 192$ mesh. In this manner the rising bubble maintains its terminal velocity on the way to disengagement, while the initialized proximity of the free surface at which the bubble bursts reduces simulation time while preserving proper

bubble-cap formation. Non-uniform spacing is used in the xy -plane, with the filter scale $\Delta = 350 \mu\text{m}$ prevailing in the vicinity of the bubble bursting and coarser mesh spacing at the outer fringes to suppress wall effects, with the xy -plane spanning $8d_e \times 8d_e$.

Table 6

Error norms on the unresolved surface tension closure term reconstructed from a snapshot of the TK96 spilling breaker simulation performed in 2D.

| | L_1 | L_2 | L_∞ |
|---|-------|--------|------------|
| ϵ_{yx}/δ no SGS curvature | 1.33 | 0.106 | 73.8 |
| ϵ_{yx}/δ with SGS curvature | 0.73 | 0.0531 | 24.0 |
| ϵ_{yz}/δ no SGS curvature | 1.11 | 0.0673 | 28.0 |
| ϵ_{yz}/δ with SGS curvature | 0.64 | 0.0343 | 9.4 |

8.3. Film break-up and daughter-drop ejection

A first example of the bubble bursting event coupling bubble rise, film rupture and droplet generation is demonstrated in Fig. 8(a)–(f). The bubble cap protrudes above quiescent free-surface level, such that the film between the free surface and the bubble upper surface features a significant mean curvature. The significant protrusion of the draining film above the quiescent free surface level results in a film liquid volume for film rupture and break-up (shown in Fig. 8c) that would be larger than for a similar bubble size in water.

A 2D slice through the geometric centre of the bubble is shown in Fig. 8b. The lower regions of the bubble, the top and the free surface centrally above it have relatively smooth spatial variations in curvature that are only small multiples away from that corresponding to the equivalent-volume sphere curvature. In the azimuth corresponding to minimum film thickness shown in Fig. 8b, the free surface and the bubble surface bounding the film feature maximum curvature in the flow domain. The high curvature is primarily azimuthal, and persists into the film break-up shown in Fig. 8c. The result shown in Fig. 8c is an illustrative example of surface tension-induced flow instability initiating 3D interface wrinkling even in non-turbulent flows.

Fig. 8c shows the bubble bursting to occur due to film disintegration rather than to film roll-up, with the bulk of the film fracturing occurring towards the outer edge of the film (as compared to towards the axis of symmetry). Randomness in the film drainage makes it difficult to delineate physically sensible phenomenology from spurious numerical artefacts. The distinction between lack of simulation fidelity due to resolution limitations and due to poor-quality numerics is even more difficult to make. As supporting evidence for the proposition that (subject to resolution limits that result in significant coarse-graining) the LEIS is able to realistically simulate the bubble bursting event, Fig. 8g–i show experimental images from Divoux et al. [9] and Resch [37] that show a noticeable large body of film liquid still intact, despite the surrounding film having vanished. Fig. 8i shows a snapshot hologram of film drops created by bubble bursting, captured experimentally by Resch [37]. These experimental observations validate the numerical model, showing a qualitatively realistic reproduction of a sample realization of the bubble bursting event.

One outcome of the bubble bursting simulation shown in Fig. 8d that merits further investigation is that the largest simulated film drop is of mm-scale – 3 mm in this case. One known experimental measurement for the size of the largest film drop from air/water systems is that drops are up to 0.7 mm in diameter for a 10 mm air bubble in distilled water [1]. We note that viscous resistance in the liquid film in the simulated case may contribute to more liquid remaining in the bubble cap when rupture does occur, resulting in a larger maximum film drop. However, we also acknowledge that the simulation is pushing the limits of mesh resolution, and so the predicted maximum film drop size may well be overestimated due to this. In any case, Fig. 8d shows the maximum film drop size to be at least similar, within an order of magnitude, and the size of the smaller simulated film drops are of comparable magnitude to those documented in the literature. The largest film drop in

Fig. 8d is shown to have been ejected some distance above the height at which the film rupture occurred, with a leftward trajectory away from the central axis. This means that the rising jet is not impeded by film remnants.

Post-processing of Fig. 8d yields 358 drops, of which 201 are identified as sub-filter in nature. Typical numbers from experiment for the number of film droplets generated by film rupture in the bubble bursting event are $O(10^2)$; for the air–water system, results summarized in [13] predict that about 100 droplets should be generated from the film liquid (on a time scale well before the jet break-up event). Given the filter width is one to two orders of magnitude larger than experimentally observed film thicknesses, film drop sizes are overestimated. Mesh refinement and improved numerics for tracking thin-fluid regions will be applied in the future, to enable better quantitative comparison of drop-size distributions towards extrapolating out grid-independent estimates.

8.4. Turbulence generation and LEIS

As shown in Fig. 8d, the droplets generated by film break-up are ejected well above the free surface. The number of droplets and ejection velocities involved result in turbulence generation in the gas-sided flow. In interfacial flows, turbulence may indeed be bubble- or droplet-based, rather than only shear-based as prevails in single-phase turbulent flows. The characteristic lengths and velocities of the small-scale vortical structures depend on the population balance of the inclusions – whether they be droplets ejected by bursting, or bubble populations rising to burst at the free surface in the first place.

It is worth noting that in this bubble bursting scenario where film drops are ejected prior to the ejection of jet drops, the drops are ejected upward at significant velocity from a film that has little translational velocity associated with it. This is because the velocities of the drops – and hence the turbulence intensity generated by them – are highly influenced by energy conservation associated with the film break-up. While errors in surface tension modelling may saturate with adequate resolution, it is evident from the size of the drops and filaments in Fig. 8d (as well as the drop size distributions quoted in [13]) that discretization curvature estimates generated in the film break-up zone during the course of the simulation may be poor. In such areas of the flow, SGS curvature modelling may contribute to better predicting the energy balance and hence the velocities at which drops are ejected upwards.

Well beyond the film drop ejection event, the LEIS remains robust, with Fig. 8e showing the eventual re-coalescing of the largest droplet with the free surface. At this stage, significant populations of smaller droplets still remain airborne (visible upon close inspection of Fig. 8e). Over time, these smaller droplets also eventually fall back to the free surface, and the waves induced by the impacts are damped out, such that Fig. 8f shows an essentially quiescent free surface to be recovered. This is an important outcome in verifying the settings in the SGS surface tension model to be robustly versatile, and the LEIS overall to be stable.

9. Conclusion

The work presented here is the first documented effort undertaken in the sub-grid scale modelling of unresolved surface tension, and represents a step forward from the identification of SGS surface tension made by the authors and by other researchers. The procedure represents a sub-grid scale model in the true sense of the term; it is not a discretization scheme, nor does the concept of an order of accuracy apply.

Technically, the procedure is based on the analysis of variations in curvature resulting from using different filtering techniques and

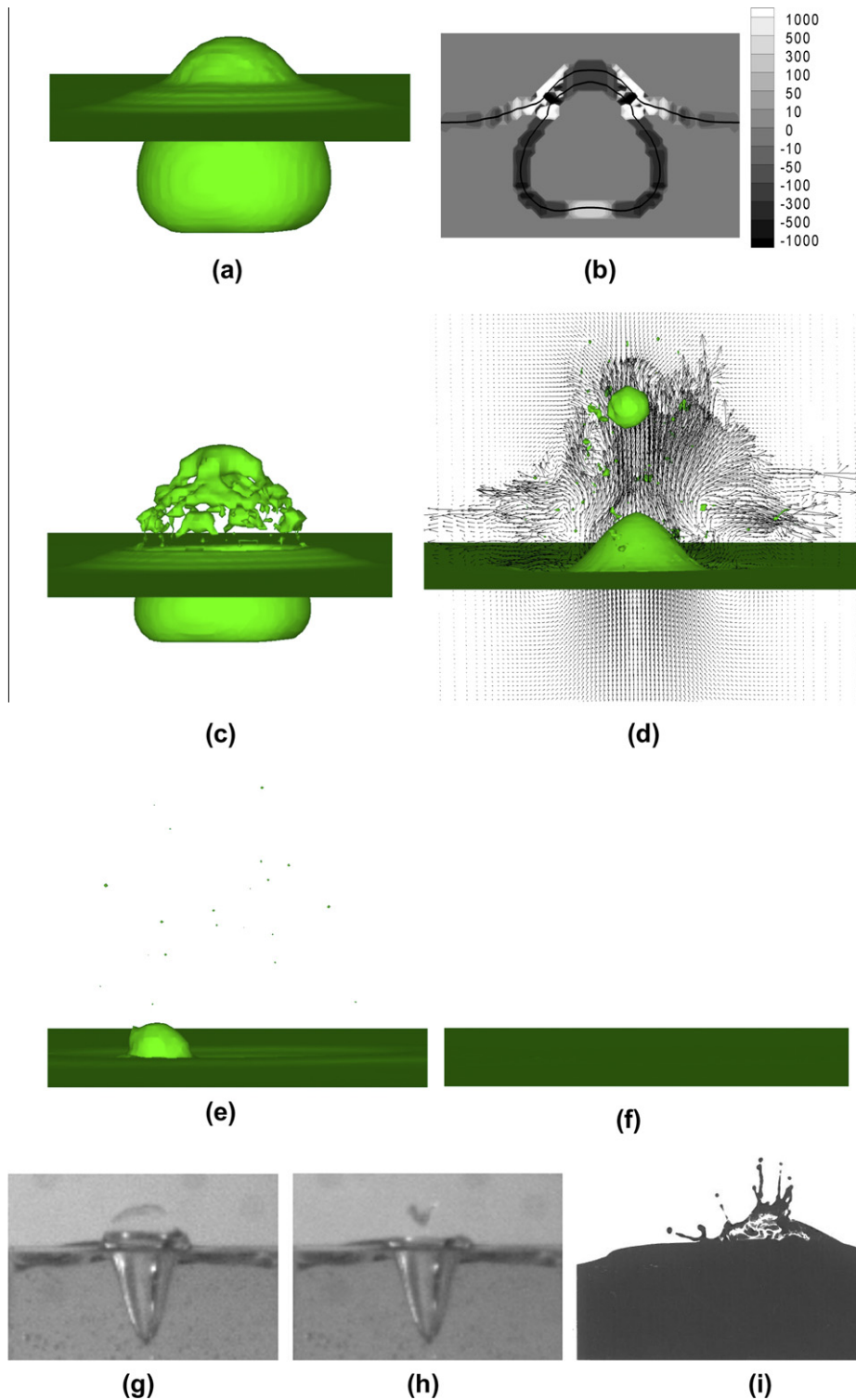


Fig. 8. Bubble bursting at a free surface: (a) in simulation, rise of bubble through free surface level initiates film drainage from the bubble cap; (b) unfiltered curvature $\kappa^{(A)}$ for the interface configuration presented in (a); (c) simulated 3D film break-up in the form of disintegration that generates a spectrum of film droplet radii; (d) velocity field in 2D slice through geometric centre of flow, showing turbulence generation above the free surface in the aftermath of bubble bursting; (e) re-coalescence of the largest film drop with the free surface, while a significant population of smaller droplets remain airborne; (f) restoration of free surface smoothness after all droplets have re-coalesced with the free surface, and after the surface waves resulting from those impacts have damped out; (g) and (h) experimental images from Divoux et al. [9] showing a large body of film liquid still intact, despite the surrounding film having disappeared; (i) snapshot hologram of film drops created by bubble bursting, as captured by Resch [37]. [(Panels (g) and (h) in this Figure) Reprinted from Fig. 1, Phys. Rev. E Vol. 77, (2008), 056310 with permission from Divoux et al. [9]. Copyright 2008 by the American Physical Society. Readers may view, browse, and/or download material for temporary copying purposes only, provided these uses are for noncommercial personal purposes. Except as provided by law, this material may not be further reproduced, distributed, transmitted, modified, adapted, performed, displayed, published, or sold in whole or part, without prior written permission from the American Physical Society. [<http://pre.aps.org/abstract/PRE/v77/i5/e056310>]. [(Panel (i) in this Figure) Reprinted from Fig. 10 from "Resch [37], Copyright 1986 by D. Reidel Publishing Company", with kind permission from Springer Science+Business Media B.V., and F. Resch.]

filter widths. Alternative discretization-based and direct-filtering techniques are used to generate coarse-filter curvature estimates, and the estimates are compared. Consistent variations between the different filtering techniques across coarser filters represent detection of legitimate instances of SGS curvature. In contrast, inconsistent variations between the different filtering techniques across coarser filters represent detection of spurious parasitic modes. Based on this model action, unresolved surface tension contributions predicted by the model can act to smooth spatial curvature variations and dampen parasitic modes, and can alternatively restore sub-grid scale interface deformations when super-grid scale resolution underpredicts curvature. The proposed sub-grid scale curvature model requires as a prerequisite a discretization-based scheme that is robustly convergent to ensure that variations in curvature with changing filter width are consistent with the true variations in curvature. Substantial improvements in curvature and surface force estimation are demonstrated at low to medium grid resolutions, while in the high-resolution limit $\kappa^{SGS} \rightarrow 0$ can be achieved.

Although the model is intuitively best suited for surface tension-dominated flows, it may actually be more useful for the LEIS of turbulent interfacial flows, supporting discretization schemes for better capturing free surface wrinkling, jet atomization and large bubble breakup. For jet atomization and large bubble breakup featuring a broadband spectrum of interfacial scales, the smallest topology features (wrinkles, sheets, etc.) can be resolved by less than a dozen of mesh cells. Clearly, the improvements in surface tension calculation achieved by the present SGS model will enable interfacial flow simulation to retain more topology features using available computing resources.

This piece of work should motivate additional research efforts towards improved heuristics for prescribing SGS curvature treatments, but ultimately, more mathematical rigour should be employed to transcend the heuristics.

Acknowledgments

The authors acknowledges use of the supercomputing facilities at the National Computing Infrastructure www.nci.org.au. PL was supported by the CSIRO Energy Transformed Flagship. The AS-COMP participation was made possible via the EU THINS research project of the Euratom 7th Framework Programme. The authors would also like to thank the reviewers for motivating model improvements that have enhanced the paper, as well as Emeritus Professor George Yadigaroglu (ETH-Zürich) for his inspiration and his efforts in proof-reading the manuscript.

Appendix A. Volume-Of-Fluid (VOF) Interface Tracking and CWVA filtering

Mass conservation in incompressible flow enables the generic equation for fluid phase mass conservation to be re-expressed as a statement of Lagrangian invariance [21]

$$\frac{\partial \rho}{\partial t} + \mathbf{U} \cdot \nabla \rho = 0. \quad (84)$$

Because density remains constant along the trajectory of a fluid particle in incompressible flow, a similar statement can be generated for a fluid phase indicator function:

$$\frac{\partial C}{\partial t} + \mathbf{U} \cdot \nabla C = 0, \quad (85)$$

which is a standard transport equation for the phase indicator function, which is valid in the continuum limit. Incompressible flow in the continuum limit is invoked here to transform Eq. (85) into conservation form [38,21]

$$\frac{\partial C}{\partial t} + \nabla \cdot (\mathbf{U}C) = C \nabla \cdot \mathbf{U}. \quad (86)$$

Using Eq. (6) to eliminate the right-hand side divergence correction term [38] and then applying spatial filtering yields

$$\frac{\partial \bar{C}}{\partial t} + \nabla \cdot (\bar{\mathbf{U}}\bar{C}) = 0. \quad (87)$$

(This of course assumes equidistant grids, indeed, otherwise convolution errors need to be accounted for.) The spatial filtering transforms the Heaviside phase indicator function into the fractional volume indicator function of the VOF method. In addition, Eq. (87) is the final form of the statement of volume conservation from which the geometric flux-based VOF discretizations are generated. The geometric VOF methods discretize Eq. (87) directly through the construction of geometric flux volumes.

The VOF method can be linked back to the equation governing mass conservation in multi-fluid flow by rearranging Eq. (3) in its spatially-filtered form as

$$\bar{C} = \frac{\bar{\rho} - \rho_L}{\rho_G - \rho_L} \quad (88)$$

(similar for the unfiltered form), and substituting into Eq. (87) to yield the filtered equation for species mass conservation

$$\frac{\partial \bar{\rho}}{\partial t} + \nabla \cdot (\bar{\mathbf{U}}\bar{\rho}) = 0. \quad (89)$$

Rearranging the formula for the Favre averaging filtered velocity $\tilde{\mathbf{U}}$

$$\bar{\rho}\tilde{\mathbf{U}} = \bar{\rho}\tilde{\mathbf{U}} \quad (90)$$

and substituting into Eq. (89) yields

$$\frac{\partial \bar{\rho}}{\partial t} + \nabla \cdot (\bar{\mathbf{U}}\bar{\rho}) = \frac{\partial \bar{\rho}}{\partial t} + \nabla \cdot (\bar{\rho}\tilde{\mathbf{U}}) = 0, \quad (91)$$

as noted in [50]. Invoking Eq. (88) enables the VOF advection problem to be recast in terms of the CWVA velocity:

$$\frac{\partial \bar{C}}{\partial t} + \nabla \cdot (\bar{\mathbf{U}}\bar{C}) = \frac{\partial \bar{C}}{\partial t} + \nabla \cdot (\bar{C}\tilde{\mathbf{U}}) = 0. \quad (92)$$

This proves that the CWVA filtering has no direct adverse impact on our ability to use VOF based on Eq. (92) for interface tracking in Large Eddy and Interface Simulation: the CWVA-filtered velocity can be used in the VOF module of LEIS flow solvers without any need for right-hand-side SGS closure terms to be incorporated into the VOF. [This is in contrast to the outcome that results from filtering the differential form of the transport equation, i.e. filtering Eq. (85) yields [53]

$$\frac{\partial \bar{C}}{\partial t} + \tilde{\mathbf{U}} \cdot \nabla \bar{C} = \sigma_1, \quad (93)$$

where the right-hand-side is a SGS term

$$\sigma_1 = -\nabla \cdot (\tilde{\mathbf{U}} - \tilde{\tilde{\mathbf{U}}}). \quad (94)$$

requiring closure, hence making interface tracking in LEIS based on Eq. (93) less than ideal.]

Any impact that CWVA filtering may have on VOF as an interface tracking scheme occurs more indirectly, through the effect of CWVA on the other equations with a multi-fluid flow LEIS solution algorithm. Take the example of a basic two-step projection solution algorithm for incompressible flow, where the update of velocity and pressure from timestep n to timestep $n+1$ takes the form

$$\mathbf{U}^* = \mathbf{U}^n + \delta t [\mathbf{F}_{ADV} + \mathbf{F}_{VISC} + \mathbf{F}_{GRAV} + \mathbf{F}_{TENSION}], \quad (95)$$

$$\nabla \cdot \frac{1}{\rho} \nabla p^{n+1} = \frac{1}{\delta t} \nabla \cdot \mathbf{U}^*, \quad (96)$$

$$\mathbf{U}^{n+1} = \mathbf{U}^* - \frac{\delta t}{\rho} \nabla p^{n+1}. \quad (97)$$

Derivation of the algorithm steps (95)–(97) requires invocation of incompressibility in the updated solution:

$$\nabla \cdot \mathbf{U}^n = \nabla \cdot \mathbf{U}^{n+1} = 0 \neq \nabla \cdot \mathbf{U}^* \quad (98)$$

Applying CWVA to Eq. (6) at timesteps n and $n + 1$ yields

$$\nabla \cdot \tilde{\mathbf{U}} = \nabla \cdot \frac{\rho \mathbf{U}}{\rho} = \psi \neq 0. \quad (99)$$

When applied to the velocity field at timestep n , the following momentum update $\tilde{\mathbf{U}}^*$ will also change, resulting in the observation made in [50] that any consequences of CWVA filtering can be accommodated by the RHS in Eq. (99). This change is absorbed as source/sink terms into the pressure solver (RHS of the filtered version of Eq. (96)), hence why the effect of the CWVA filtering is easily accommodated within existing solution algorithms. If the CWVA filtered velocity deviates from being solenoidal, then VOF methods can accommodate that in their geometric fluxes, and if necessary also in use of the divergence correction term as outlined in the time integration templates for VOF in [38].

References

- [1] Afeti GM, Resch FJ. Distribution of the liquid aerosol produced from bursting bubbles in sea and distilled water. *Tellus* 1990;42B:378–84.
- [2] Alajbegovic A. Large eddy simulation formalism applied to multiphase flows. In: Proceedings of ASME fluids engineering division summer meeting, New Orleans, 29 May–1 June 2001, FEDSM2001-18192.
- [3] Boris JP. On Large Eddy Simulation using subgrid turbulence models. In: Lumley JL, editor. *Whither Turbulence? Turbulence at the Crossroads: Lecture Notes in Physics*, vol. 357. Springer-Verlag; 1989. p. 344–53.
- [4] Boulton-Stone JM, Blake JR. Gas bubbles bursting at a free surface. *J Fluid Mech* 1993;254:437–66.
- [5] Brackbill JU, Zemach C, Kothe DB. A continuum method for modeling surface tension. *J Comput Phys* 1992;100:335–54.
- [6] Ferdowsi PA, Bussmann M. Second-order accurate normals from height functions. *J Comput Phys* 2008;227:9293–302.
- [7] Cummins SJ, Francois MM, Kothe DB. Estimating curvature from volume fractions. *Comp Struct* 2005;83:425–34.
- [8] Dollet B, van der Meer SM, Garbin V, de Jong N, Lohse D, Versluis M. Nonspherical oscillations of ultrasound contrast agent microbubbles. *Ultrasound Med Biol* 2008;34:1465–73.
- [9] Divoux T, Vidal V, Melo F, Geminard J-C. Acoustic emission associated with the bursting of a gas bubble at the free surface of a non-Newtonian liquid. *Phys Rev E* 2008;77:056310.
- [10] Duchemin L, Popinet S, Josserand J, Zaleski S. Jet formation in bubbles bursting at a free surface. *Phys Fluids* 2002;14:3000–8.
- [11] Fedkiw R, Aslam T, Merriman B, Osher S. A non-oscillatory Eulerian approach to interfaces in multimaterial flows (the Ghost Fluid Method). *J Comput Phys* 1999;152:457–92.
- [12] Francois MM, Cummins SJ, Dendy ED, Kothe DB, Sicilian JM, Williams MW. A balanced-force algorithm for continuous and sharp interfacial surface tension models within a volume tracking framework. *J Comput Phys* 2006;213:141–73.
- [13] Günther A, Wälchli S, Rudolf von Rohr P. Droplet production from disintegrating bubbles at water surfaces. Single vs multiple bubbles. *Int J Multiphase Flow* 2003;29:795–811.
- [14] Hardt S. An extended volume-of-fluid method for micro flows with short-range interactions between fluid interfaces. *Phys Fluids* 2005;17:100601.
- [15] Herrmann M, Gorokhovski M. An outline of an LES subgrid model for liquid/gas phase interface dynamics. In: Proc. summer program – Center for Turbulence Research 2008, Stanford.
- [16] Hirt CW, Nichols BD. Volume of fluid (VOF) method for the dynamics of free boundaries. *J Comput Phys* 1981;39:205–26.
- [17] Hnat JG, Buckmeister JD. Spherical cap bubbles and skirt formation. *Phys Fluids* 1976;19:182–94.
- [18] Jacqmin D. Calculation of two-phase Navier–Stokes flows using phase-field modeling. *J Comput Phys* 1999;155:96–127.
- [19] Jamet D, Torres D, Brackbill JU. On the theory and computation of surface tension: the elimination of parasitic currents through energy conservation in the second-gradient method. *J Comput Phys* 2002;182:262–76.
- [20] Kientzler CF, Arons AB, Blanchard DC, Woodcock AH. Photographic investigation of the projection of droplets by bubbles bursting at a water surface. *Tellus* 1954;6:1–7.
- [21] Kothe DB. Perspective on Eulerian finite volume methods for incompressible interfacial flows. In: Kuhlmann HC, Rath H-J, editors. *Free Surface Flows*. Springer-Verlag; 1998. p. 267–331.
- [22] Labourasse E, Lacanette D, Toutant A, Lubin P, Vincent S, Lebaigue O, et al. Towards large eddy simulation of isothermal two-phase flows: governing equations and a priori tests. *Int J Multiphase Flow* 2007;33:1–39.
- [23] Lakehal D. DNS and LES of turbulent multifluid flows. In: Keynote third int. symp. two-phase flow modelling and experimentation, Pisa, Italy, September 22–24, 2004.
- [24] Lakehal D. LEIS for the prediction of turbulent multifluid flows applied to thermal-hydraulics applications. *Nucl Eng Des* 2010;240:2096–106.
- [25] Liovic P, Lakehal D. Interface–turbulence interactions in large-scale bubbling processes. *Int J Heat Fluid Flow* 2007;28:127–44.
- [26] Liovic P, Lakehal D. Multi-physics treatment in the vicinity of arbitrarily deformable gas–liquid interfaces. *J Comput Phys* 2007;222:504–35.
- [27] Liovic P, Francois MM, Rudman M, Manasseh R. Efficient simulation of surface tension-dominated flows through enhanced interface geometry interrogation. *J Comput Phys* 2010:7520–44.
- [28] Liovic P, Rudman M, Liow J-L, Lakehal D, Kothe DB. A 3D unsplit-advection volume tracking algorithm with planarity-preserving interface reconstruction. *Comp Fluids* 2006;35:1011–32.
- [29] Liovic P, Lakehal D. A Newton–Krylov solver for remapping-based Volume-of-Fluid methods. *SIAM J Sci Comput* 2008;31:865–89.
- [30] Lakehal D, Liovic P. Turbulent structure and interaction with steep breaking waves. *J Fluid Mech* 2011;674:522–77.
- [31] Lopez J, Zanzi C, Gomez P, Zamora R, Faura F, Hernandez J. An improved height function technique for computing interface curvature from volume fractions. *Comput Methods Appl Mech Eng* 2009;198:2555–64.
- [32] Marchandise E, Geuzaine P, Chevaugnon N, Remacle J-F. A stabilized finite element method using a discontinuous level set approach for the computation of bubble dynamics. *J Comput Phys* 2007;225:949–74.
- [33] Moses B, Edwards C, Helenbrook B. Development of a spatially-filtered method for calculation of multiphase flow. In: Proceedings of ASME joint US–European fluids engineering conference, Montreal, July 2002, FEDSM2002-31231.
- [34] Osher S, Sethian J. Fronts propagating with curvature-dependent speed: algorithms based on Hamilton–Jacobi formulations. *J Comput Phys* 1988;79:12–49.
- [35] Raymond SB, Treat LH, Dewey JD, McDannold NJ, Hynynen K, Bacskai BJ. Ultrasound enhanced delivery of molecular imaging and therapeutic agents in Alzheimer’s Disease mouse models. *PLoS ONE* 2008;3:e2175.
- [36] Reboux S, Sagaut P, Lakehal D. Large Eddy Simulation of sheared interfacial two-fluid flow using the Variational Multiscale Approach. *Phys Fluids* 2006;18:105105-1–105105-15.
- [37] Resch F. Oceanic air bubbles as generators of marine aerosols. In: Monahan EC, MacNiocaill G, editors. *Oceanic Whitecaps and their role in air–sea exchange processes*. Reidel Dordrecht; 1986. p. 101–12.
- [38] Rider WJ, Kothe DB. Reconstructing volume tracking. *J Comput Phys* 1998;141:112–52.
- [39] Rudman M. A volume-tracking method for incompressible multi-fluid flows with large density variations. *Int J Numer Methods Fluids* 1998;28:357–78.
- [40] Sagaut P. *Large Eddy Simulation for incompressible flows*. Springer; 2009.
- [41] Spiel DE. A hypothesis concerning the peak in film drop production as a function of bubble size. *J Geophys Res* 1997;102:1153–61.
- [42] Spiel DE. On the births of film drops from bubbles bursting on seawater surfaces. *J Geophys Res* 1998;103:24907–18.
- [43] Sussman M, Ohta M. A stable and efficient method for treating surface tension in incompressible two-phase flow. *SIAM J Sci Comput* 2009;31:2447–71.
- [44] Sussman M, Ohta M. High-order techniques for calculating surface tension forces. *Int Ser Numer Math* 2009;154:425–34.
- [45] Sussman M, Puckett EG. A coupled Level Set and Volume-of-Fluid method for computing 3D and axisymmetric incompressible two-phase flows. *J Comput Phys* 2000;162:301–37.
- [46] Sussman M, Smereka P, Osher S. A level set approach for computing solutions to incompressible two-phase flow. *J Comput Phys* 1994;114:146–59.
- [47] Tho P, Manasseh R, Ooi A. Cavitation microstreaming in single and multiple bubble systems. *J Fluid Mech* 2007;576:191–223.
- [48] Ting FCK, Kirby JT. Dynamics of surf-zone turbulence in a spilling breaker. *Coastal Eng* 1996;27:131–60.
- [49] Toutant A, Chandris M, Jamet D, Lebaigue O. Jump conditions for filtered quantities at an under-resolved discontinuous interface. Part 1: Theoretical development. *Int J Multiphase Flow* 2009;35:1100–18.
- [50] Toutant A, Labourasse E, Lebaigue O, Simonin O. DNS of the interaction between a deformable buoyant bubble and a spatially decaying turbulence: a priori tests for LES two-phase flow modeling. *Comp Fluids* 2008;37:877–86.
- [51] TransAT handbook series. Equations algorithms, turbulence modelling simulation, multiphase flow modelling. Version 2.3.0, Ed. Switzerland: ASCOMP GmbH; 2010. <www.ascomp.ch>.
- [52] Vincent S, Caltagirone J-P. Test-case number 10: parasitic currents induced by surface tension (PC). In: Jamet D, Lebaigue O, Lemonnier H editors. *Test-cases for interface tracking methods*; 2004. p. 79–84.
- [53] Vincent S, Larocque J, Lacanette D, Toutant A, Lubin P, Sagaut P. Numerical simulation of phase separation and a priori two-phase LES filtering. *Comp Fluids* 2008;37:898–906.
- [54] Watanabe Y, Saeki H, Hosking RJ. Three-dimensional vortex structures under breaking waves. *J Fluid Mech* 2005;545:291–328.
- [55] Williams MW, Puckett EG, Kothe DB. Convergence and accuracy of continuum surface tension models. In: Shyy W, Narayanan R editors. *Fluid dynamics at interfaces*; 1999. p. 294–305.